# Nanostructured $Li_2S$ Cathodes for Silicon-Sulfur Batteries

*Hamid Mollania,* [a,b] *Chaoqi Zhang,* [b] *Ruifeng Du,* [b] *Xueqiang Qi,*,*[c] *Junshan Li,* [d] *Sharona Horta,* [e] *Maria Ibañez,* [e] *Caroline Keller,* [f] *Pascale Chenevier,* [f] *Majid Oloomi-Buygi,*,*[a] *and Andreu Cabot *,*[b,g]

[a] Ferdowsi University of Mashhad, Department of Electrical Engineering, Mashhad 9177948974, Iran. E-mail: m.oloomi@um.ac.ir

[b] Catalonia Institute for Energy Research - IREC, Sant Adrià del Besòs, Barcelona 08930, Spain. E-mail: acabot@irec.cat

[c] College of Chemistry and Chemical Engineering, Chongqing University of Technology, Chongqing 400054, China. E-mail: xqqi@cqut.edu.cn

[d] Institute for Advanced Study, Chengdu University, 610106, Chengdu, China.

[e] Institute of Science and Technology Austria (ISTA), Am Campus 1, Klosterneuburg 3400, Austria.

[f] Université Grenoble Alpes, CEA, CNRS, IRIG, SYMMES, STEP, 38000 Grenoble, France.

[g] ICREA, Pg. Lluís Companys 23, 08010 Barcelona, Catalonia, Spain.

* Corresponding authors.

## Abstract

Lithium-sulfur batteries (LSBs) are regarded as an advantageous option for meeting the growing demand for high-energy density storage, but their commercialization relies on solving the current limitations of both sulfur cathodes and lithium metal anodes. In this scenario, the implementation of lithium sulfide ($Li_2S$) cathodes compatible with alternative anode materials such as silicon has the potential to alleviate the safety concerns associated with lithium metal. In this direction, here we report a sulfur cathode based on $Li_2S$ nanocrystals grown on a catalytic host consisting of CoFeP nanoparticles supported on tubular carbon nitride. Nanosized $Li_2S$ is incorporated into the

host by a scalable liquid infiltration-evaporation method. Theoretical calculations and experimental results demonstrate that the CoFeP-CN composite can boost the polysulfide adsorption/conversion reaction kinetics and strongly reduce the initial overpotential activation barrier by stretching the Li−S bonds of $Li_2S$. Besides, the ultra-small size of the $Li_2S$ particles in the $Li_2S$-CoFeP-CN composite cathode facilitates the initial activation. Overall, $Li_2S$-CoFeP-CN electrodes exhibit a low activation barrier of 2.56 V, a high initial capacity of 991 mAh $g_{Li_2S}^{-1}$, and an outstanding cyclability with a small fading rate of 0.029% per cycle over 800 cycles. Moreover, Si/$Li_2S$ full cells are assembled using the nanostructured $Li_2S$-CoFeP-CN cathode and a pre-lithiated anode based on graphite-supported silicon nanowires. These Si/$Li_2S$ cells demonstrate high initial discharge capacities above 900 mAh $g_{Li_2S}^{-1}$ and a good cyclability with a capacity fading rate of 0.28% per cycle over 150 cycles.

## Keywords

Carbon nitride, lithium–sulfur battery, lithium sulfide cathode, metal phosphide, polysulfides, silicon nanowire, sulfur cathode.

## Introduction

As we transition to an electric transportation system and replace fossil fuels with renewables, enhanced high energy density batteries for electric vehicles and eco-friendly dispatching of intermittent renewables in smart grids are required. Lithium-sulfur batteries (LSBs), with an average discharge voltage of 2.2 V and a high theoretical specific energy density of 2600 Wh $kg^{-1}$ are widely regarded as a viable option for addressing the ever-growing energy storage demands.[1,2] Despite the benefits of LSBs, the low electrical conductivity of sulfur and lithium sulfide, the solubility and related shuttle effect of lithium polysulfides (LiPSs), and the safety concerns

associated with lithium anodes prevent their commercialization.[3,4] To overcome these limitations, it is imperative to devise sulfur hosts that possess high electrical conductivity, large polar areas capable of binding LiPS, catalytic activity to expedite their conversion, and porous architectures that can accommodate the volumetric fluctuations of sulfur while simultaneously ensuring appropriate ionic and electronic transportation.[5-7]

At the anode side, lithium metal can be replaced by graphite, silicon,[8,9] tin,[10] or transition metal oxides,[11] among others. In this case, the lithium-free anode needs to be coupled with a sulfur cathode made of the fully-lithiated form of sulfur ($Li_2S$). $Li_2S$ offers a high specific capacity of 1166 mAh $g^{-1}$, and since it is the least dense form of lithiated sulfur, its use can avoid the problems associated with the large volume expansion of sulfur. However, its hydrolysis susceptibility and high activation barrier have limited the performance of LSBs assembled using $Li_2S$ instead of S.[1,12] The challenges encountered have led to a vast majority of LSB research focusing on the use of S instead of $Li_2S$ for LSB assembly, thereby imposing significant constraints on the anode. The high initial $Li_2S$ activation barrier, which may reach up to 1 V and lead to the decomposition of the ether-based electrolyte, can be overcome by exploiting its significant dependence on the $Li_2S$ crystallinity and particle size, i.e. using $Li_2S$ domains with nanometric dimensions.[13,14] However, most laboratory approaches to synthesize nanoscale $Li_2S$ use extremely flammable organolithium reagents and are not cost-competitive with commercial $Li_2S$.[15] As an alternative, $Li_2S$ nanoparticles can be produced via a simple and safe infiltration-evaporation approach due to the high solubility of $Li_2S$ in ethanol.[16] In this direction, the dissolution of commercially available $Li_2S$ in anhydrous ethanol and its recrystallization into nanosized $Li_2S$ is the most viable alternative.

Several porous conductive carbonaceous matrices with high specific surface area (SSA), such as microporous carbons,[17] carbon nanofibers,[18] and carbon nanotubes,[19] have been used as $Li_2S$ hosts at the LSB cathode. Since LiPSs are inherently polar species, coating the substrates with polar materials, such as metal oxides, sulfides, nitrides, and phosphides, contributes to trapping LiPSs while at the same time activating their redox reactions.[20] Among them, transition metal phosphides (TMP) stand out owing to their high electrical conductivity, excellent LiPS absorption, low cost of phosphorous, abundance, and potential for facile synthesis. Besides, beyond promoting the nucleation of $Li_2S$, TMPs are highly efficient in reducing the $Li_2S$ decomposition energy by facilitating its change of phase.[20,21]

As a high surface area and porous carbon-based support, graphitic carbon nitride (g-$C_3N_4$), a lightweight semiconductor made of continuous tri-s-triazine building blocks, possesses particularly appealing electrical conductivity, polar surfaces, catalytic capabilities, and low interface impedance.[22,23] In particular, the presence of pyridinic-N within g-$C_3N_4$ provides Lewis-base sites able to chemically bind LiPS.[24,25] Combining high SSA g-$C_3N_4$ tubes with TMP nanoparticles can be an effective strategy for encapsulating $Li_2S$ while at the same time maximizing the dispersion of TMP and preventing their aggregation, thus boosting the LSB performance.

The synthesis of TMP-based composites frequently relies on gas-solid processes using sodium hypophosphite or ammonium dihydrogen phosphate as a source of phosphorous, releasing hazardous phosphine gas.[26] On the other hand, solution-based physical self-assembly approaches require multiple steps and generally result in poor TMP dispersions due to the poor coupling of g-$C_3N_4$ with TMPs.[27] In comparison to the physical self-assembly approaches, the direct solution growth of TMPs on the surface of the g-$C_3N_4$ can be much simpler, safer, environmentally friendly,

and effective.[28] Besides, the use of mild conditions for the synthesis of CoFeP nanocrystals in the presence of the g-$C_3N_4$ prevents damaging the g-$C_3N_4$ structure thus maintaining its electrochemical properties. Therefore, developing an in situ liquid-phase synthesis strategy to nucleate bimetallic phosphide CoFeP nanocrystals with fine particle sizes on the g-$C_3N_4$ surface is a worthy endeavor.

Motivated by the aforementioned developments, herein we detail a simple method to in situ embed bimetallic CoFeP nanoparticles into porous g-$C_3N_4$ nanotubes to produce CoFeP-CN composites. Such CoFeP-CN composites are thoroughly characterized and used as $Li_2S$ hosts. $Li_2S$-CoFeP-CN composites with ultra-small $Li_2S$ nanoparticles are then synthesized using a facile, practical, and safe liquid infiltration-evaporation approach. Computational tools are used to determine the role of the CoFeP-CN host on $Li_2S$ decomposition. Besides, the electrochemical performance of $Li_2S$-CoFeP-CN cathodes is experimentally investigated using half cells, and their cycle stability and rate capability are put through an extensive testing process. Finally, full cells based on $Li_2S$-CoFeP-CN cathodes and pre-lithiated Si anodes are assembled and tested.

## Experimental Section

**Synthesis of g-$C_3N_4$ tubes**. Melamine (99%, Acros Organics) and cyanuric acid (99%, Acros Organics) were used to self-assemble g-$C_3N_4$ nanotubes.[22] In a typical synthesis, the solution of melamine and deionized water (1 g melamine in 300 mL of deionized water) was added to the cyanuric acid solution (1 g cyanuric acid in 300 mL deionized water) and the final solution remained under stirring at 80 °C for 1.5 hours. After centrifuging and washing with 80 °C deionized water, the product was dispersed in deionized water and stored in the fume hood until the precursors settled. The precipitated product was then freeze-dried for 48 hours. After that, the

final product was calcined at 520 °C for 2h with a heating rate of 2 °C/min under Ar atmosphere to obtain tubular g-$C_3N_4$.

**Synthesis of CoFeP-CN.** The CoFeP-CN composite was produced with a one-pot heating-up reaction. In a typical synthesis, 100 mg of as-prepared g-$C_3N_4$ was added to the mixture of 4.8 g (10 mmol) of 1-hexadecylamine (HDA, 90%, Acros Organics), 10 mL of 1-octadecene (ODE, 90%, ACROS Organics) and 5.2 mL (10 mmol) of triphenyl phosphite (99%, ACROS Organics). Then the system was degassed under a vacuum and continued stirring at 150 °C for 2 h. After that, the atmosphere changed to argon, and the mixture of 390 mg (2 mmol), $Fe(CO)_5$ (Sigma Aldrich), and 384 mg (1 mmol) $Co_2(CO)_8$ (95%, ACROS Organics) in 4 mL ODE was injected into the system. Meanwhile, the temperature was increased to 290 °C with a 5 °C/min heating ramp and remained at 290 °C under homogenous stirring for 1h. Then the heating source was removed and the system was allowed to cool down to 200 °C gradually. Afterward, the solution was cooled down quickly to room temperature using the water bath. The product was centrifuged and washed several times with the solution of acetone and chloroform and then dried for one night in a 65 °C oven. Finally, to eliminate organics, the dry product was then annealed under argon for 2 h at 400 °C and a heating ramp of 5 °C/min (abbreviated as CoFeP-CN).

**Synthesis of $Li_2S$-CoFeP-CN, $Li_2S$-CN, and $Li_2S$-KB-Co.** To synthesize the $Li_2S$-CoFeP-CN, $Li_2S$-CN, and $Li_2S$-KB-Co composites, 115 mg of lithium sulfide ($Li_2S$, 99.9%, Alfa Aesar) was dissolved in 5 mL anhydrous ethanol (EtOH, ≥99.8%, VWR Chemicals) and the solution left under stirring overnight at room temperature. $Li_2S$ is moisture sensitive, and when it reacts with water, it produces LiOH, which precipitates in ethanol. The ethanol used had a maximum moisture content of 0.003% and all the procedure was done inside the Ar-filled glove box with a 0.0 ppm $H_2O$ level to prevent hydrolysis of $Li_2S$. The obtained $Li_2S$-EtOH solution was pale yellow and no

LiOH was observed as precipitated in the solution. Afterward, the $Li_2S$-EtOH solution was heated up to 50 °C and slowly injected into a glass bottle containing 55 mg of the as-synthesized host so that all the materials get completely wet. During the injection, a low vacuum (~60 mbar) was employed and the temperature of the glass bottle remained around 100 °C using an oil bath. Due to the vacuum, the solution penetrated into the small pores of the host and ethanol rapidly evaporated, which might reduce the size of $Li_2S$ that was nucleated on the host. Finally, the product was completely dried for 2 h at 200 °C and a heating ramp of 15 °C/min. It should be mentioned that the host and glass bottle were dried at 100 °C for 12 hours in the vacuum oven before being used.

## Results and Discussions

Porous graphitic carbon nitride (g-$C_3N_4$) nanotubes were synthesized from the reaction of cyanuric acid and melamine (1:1 molar ratio) and annealing the resulting powder at 520 °C in an environment of argon (see the Experimental Section in the Supporting Information for details). Transmission electron microscopy (TEM) analysis confirmed the porous and tubular architecture of the obtained g-$C_3N_4$ (Figure 1a). Powder X-ray diffraction (XRD) patterns confirmed the orthorhombic crystal phase of g-$C_3N_4$ (PDF JCDD 00-066-0813, Figure 1b).

CoFeP-CN composites were synthesized using a one-pot heating-up process based on the reaction of Co and Fe precursors with ambient-stable triphenyl phosphite (TPOP)[29] in the presence of pre-synthesized g-$C_3N_4$ nanotubes, as schematized in Figure 1c. Scanning electron microscopy (SEM) images and energy dispersive X-ray spectroscopy (EDX) analysis show the g-$C_3N_4$ nanotubes decorated by CoFeP particles (Figure 1d and S1). The XRD pattern of CoFeP-CN reveals the presence of both g-$C_3N_4$, with a main diffraction peak at 27.5° belonging to the (002) family planes, and CoFeP with the orthorhombic crystal phase (JCPDS 01-082-5970) displaying

main peaks at 40.5° and 51.7° associated with the (112) and (020) planes (Figure 1e). TEM analysis shows the CoFeP-CN composite to have a porous structure. CoFeP nanocrystals on the g-$C_3N_4$ surface are seen as black ellipsoids with average dimensions of around 15 × 5 nm (Figure 1f). Additionally, high-resolution TEM (HRTEM) images combined with power spectrum (FFT) analysis of one of the CoFeP nanoparticles confirm the Pnma space group of CoFeP (Figure 1g). High-angle annular dark-field-scanning transmission electron microscopy (HAADF-STEM), EDX compositional maps, and annular dark-field-scanning-STEM (ADF-STEM) images verified the uniform distribution of CoFeP on g-$C_3N_4$ (Figure 1h and S2).

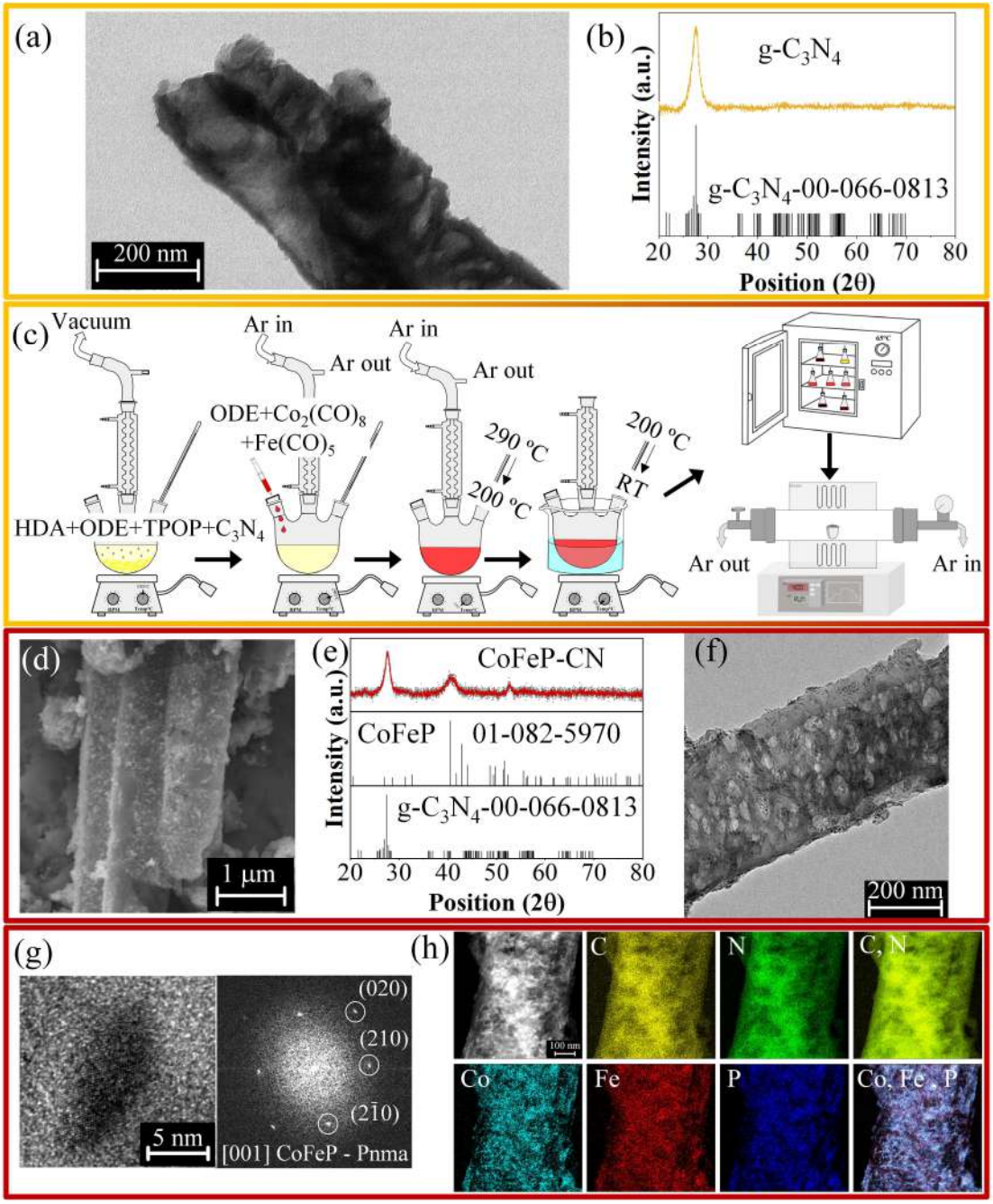


**Figure 1.** (a) TEM image of g-$C_3N_4$. (b) XRD pattern of g-$C_3N_4$. (c) Schematic of the CoFeP-CN preparation method. (d) SEM image of CoFeP-CN composite. (e) XRD pattern of CoFeP-CN. (f) TEM image of the CoFeP-CN composite. (g) HRTEM image and corresponding power spectrum (FFT) from CoFeP nanoparticles supported on g-$C_3N_4$. (h) HAADF-STEM images and EDX compositional maps of CoFeP-CN.

After the synthesis of the CoFeP-CN composite, $Li_2S$-CoFeP-CN composites were produced by injecting an anhydrous ethanol solution of $Li_2S$ ($Li_2S$–EtOH) into a flask containing the CoFeP-CN host within an Ar-filled glovebox (see details in the Supporting Information, Figure 2). To shorten the $Li_2S$ growth time, the $Li_2S$-EtOH solution was heated up to 50 °C and it was slowly injected into the flask maintained at 100 ºC. Using a low vacuum (~60 mbar) during the injection enhanced the solution infiltration into the small pores of the CoFeP-CN powder. In these relatively high temperatures and low-pressure conditions, EtOH evaporates very fast, resulting in heterogeneous $Li_2S$ nanoparticle nucleation on the CoFeP-CN surface.

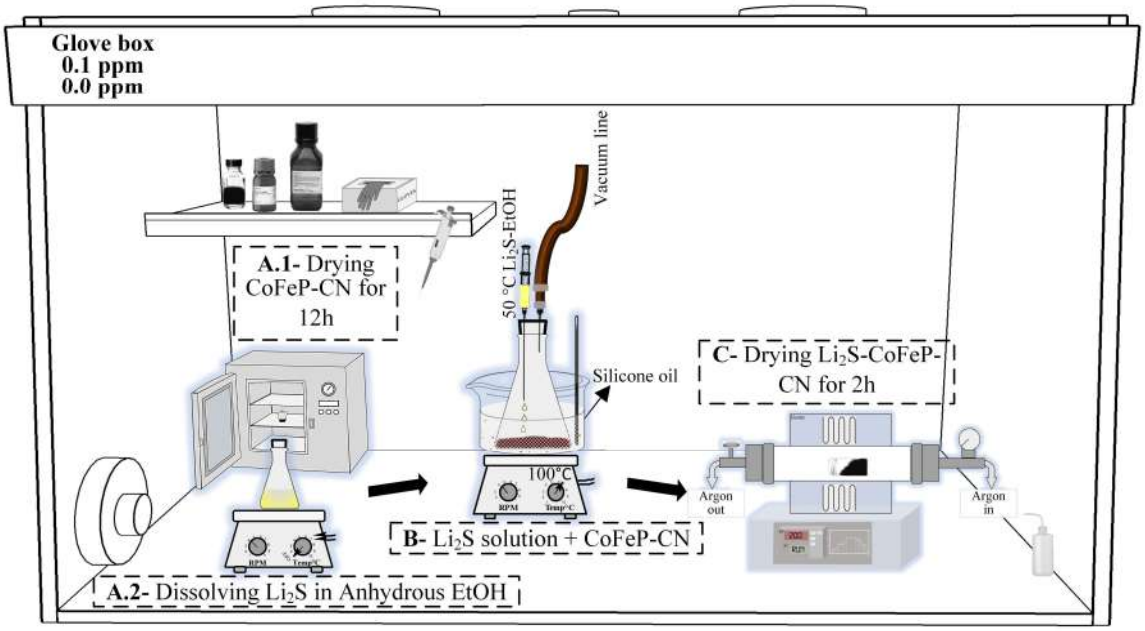


**Figure 2.** Schematic illustration of the $Li_2S$-CoFeP-CN preparation method.

SEM analysis showed that the introduction of $Li_2S$ preserved the tubular architecture of the CoFeP-CN composite (Figure 3a,b). Additionally, SEM-EDX elemental maps show a homogeneous distribution of $Li_2S$ throughout the composite host (Figure 3c). The XRD pattern of the $Li_2S$-CoFeP-CN composite displays the fingerprint of the cubic phase of $Li_2S$ (JCPSD 01–077–2874, Figure 3d) matching the commercial $Li_2S$ used as a precursor. The wide band at low

angles in the XRD pattern is related to the use of Kapton tape to protect the samples from the air during measurement. The $Li_2S$ obtained from the dissolution of commercial $Li_2S$ in EtOH and its posterior nucleation on the CoFeP-CN exhibits much weaker and broader XRD peaks than the commercial $Li_2S$ precursor (Figure 3e). This indicates that the size and crystallinity of the new $Li_2S$ domains are much smaller/lower than the initial $Li_2S$ particles.[30] Using the Scherrer formula,[31] the size of the recrystallized $Li_2S$ domains was quantified at about 20 nm (Figure S3). The absence of the g-$C_3N_4$ and CoFeP XRD peaks in the $Li_2S$-CoFeP-CN pattern is related to the high load of $Li_2S$ introduced. SEM-EDX elemental spectra of $Li_2S$-CoFeP-CN confirm the presence of all elements in the composite except Li which cannot be detected by EDX analysis (Figure S4). The $Li_2S$ content was calculated as 69 wt.% based on the at.% of S obtained from a large area EDX measurement (Table S1).

Thermogravimetric analysis (TGA) of $Li_2S$-CoFeP-CN and CoFeP-CN was carried out to determine the amount of CoFeP and $Li_2S$ in CoFeP-CN and $Li_2S$-CoFeP-CN composites (Figure 3f). The samples were protected under Ar atmosphere within the TGA system and the temperature increased to 300 ºC. When the atmosphere was changed to dry air, at 300 ºC, the temperature raised faster than preset as $Li_2S$ was completely and exothermically oxidized to $Li_2SO_4$.[12,14] The CoFeP-CN TGA profile shows a notable weight loss above 420 °C caused by the combustion of the carbon nitride polymer into carbon dioxide and nitrogen gases. As the temperature increases up to 750 °C, there is almost no residual g-$C_3N_4$ left behind and CoFeP has transformed to $Co_2O_3$, $Fe_2O_3$, and $P_2O_5$.[32,33] Assuming all CoFeP nanocrystals have been oxidized at the end of TGA analysis, the weight percentage of CoFeP in the CoFeP-CN composite can be calculated using equations S2 and S3 (see the Supporting Information). From these equations, the CoFeP content in the CoFeP-CN composite was estimated at around 16 wt.% which is close to the EDX results (Table S1). From

the TGA profiles, the weight fraction of $Li_2S$ in the $Li_2S$-CoFeP-CN composite was determined using two different methods (see the Supporting Information for details). In the first method, the final product of the TGA analysis in the $Li_2S$-CoFeP-CN composite is considered to be $Li_2SO_4$, $Co_2O_3$, $Fe_2O_3$, and $P_2O_5$. Under this assumption, the $Li_2S$ weight percentage was calculated using equations S4 and S5. In the second method, equation S6 was used considering only the initial and final weights in the TGA analysis of $Li_2S$-CoFeP-CN, i.e. without taking into account the transformation of the CoFeP. Owing to the moderate amount of CoFeP and its low mass change during oxidation, both methods show that the weight percentage of $Li_2S$ within $Li_2S$-CoFeP-CN is about 67%. This result is also consistent with the weight difference between the initial CoFeP-CN (55 mg) host and the loaded $Li_2S$-CoFeP-CN (168 mg) material after drying.

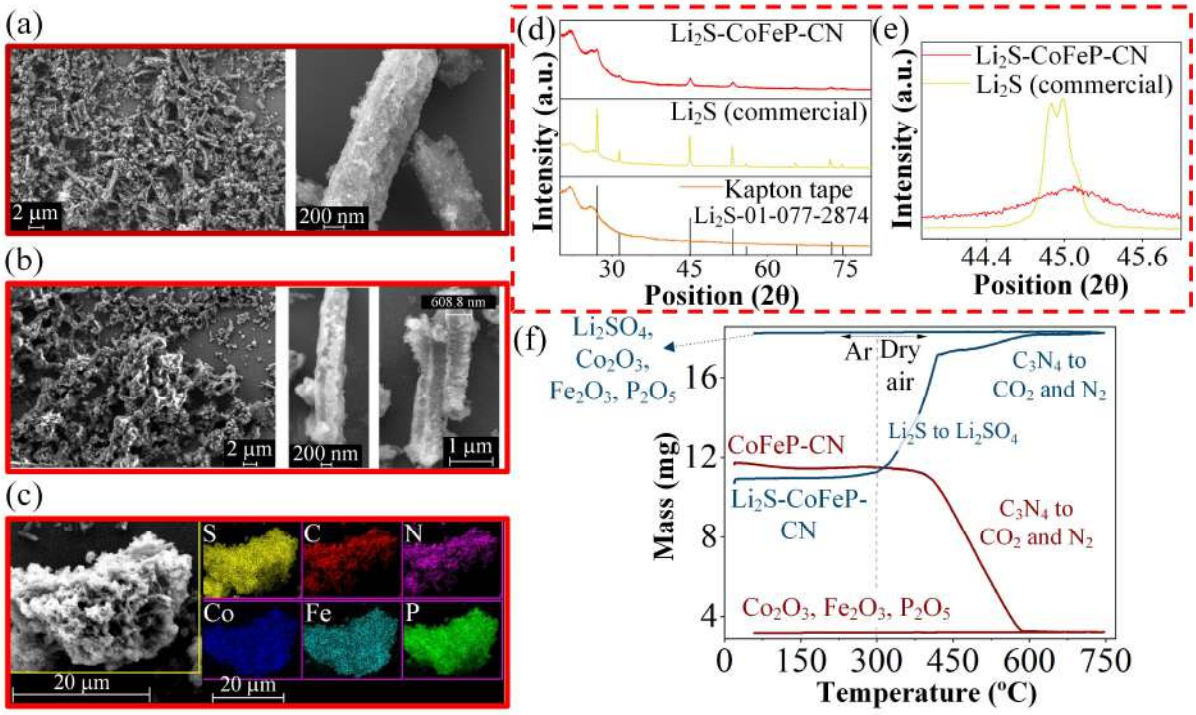


**Figure 3.** (a) SEM images of the CoFeP-CN. (b) SEM images of $Li_2S$-CoFeP-CN. (c) SEM-EDX elemental maps of $Li_2S$-CoFeP-CN. (d) XRD peaks of $Li_2S$-CoFeP-CN, commercial $Li_2S$, Kapton

tape and $Li_2S$ standard (from up to down). (e) Comparison of XRD peak at 45° for $Li_2S$-CoFeP-CN and commercial $Li_2S$. (f) TGA analysis of $Li_2S$-CoFeP-CN and CoFeP-CN.

The SSA and porosity of CoFeP-CN and $Li_2S$-CoFeP-CN samples were evaluated from $N_2$ adsorption-desorption isotherms (Figure S5). The CoFeP-CN sample exhibits a typical type IV adsorption-desorption curve with an apparent capillary condensation phenomenon.[34] The single-layer adsorption stage leads to the concave shape of the curve at low relative pressure and the inflection point indicates the start of the multilayer adsorption stage. The adsorption-desorption isotherms do not overlap and exhibit a type H3 hysteresis loop from 0.42 to 1 relative pressure ($P/P_0$), demonstrating the presence of abundant mesopores. The $Li_2S$-CoFeP-CN sample shows a type III isotherm. At a relative pressure lower than 0.7, the curve is concave without an inflection point and relatively low adsorption, which is associated with a relatively weak solid-$N_2$ interaction when compared with $N_2$-$N_2$ interactions. Adsorption increased when the relative pressure reached 0.8, and a narrow H3 hysteresis loop emerged. The capillary condensation stage of $Li_2S$-CoFeP-CN shifted to a higher relative pressure, indicating that the porosity of this sample is lower than that of the CoFeP-CN.[35,36] Furthermore, since condensation and evaporation occur at higher relative pressures for larger pores,[37] this shift also indicates that only the largest pores remained after introducing the $Li_2S$. The CoFeP-CN pore-size distribution, calculated using the Barret-Joyner-Halenda (BJH) model, confirms that the material is dominated by mesopores (inset of Figure S5). The average pore diameter of $Li_2S$-CoFeP-CN is higher than the CoFeP-CN composite and the mesopore volume in $Li_2S$-CoFeP-CN is substantially smaller than that of CoFeP-CN, demonstrating that $Li_2S$ was effectively impregnated into the CoFeP-CN mesoporous channels. CoFeP-CN has a Brunauer–Emmett–Teller (BET) SSA of 114.2 $m^2\ g^{-1}$ and a BJH pore volume of 0.24 $cm^3\ g^{-1}$. This high SSA and pore space are advantageous for the nucleation of $Li_2S$

particles. In contrast, $Li_2S$-CoFeP-CN has a much lower SSA, 14.8 $m^2\ g^{-1}$, and pore volume, 0.11 $cm^3\ g^{-1}$, which is consistent with the introduction of $Li_2S$ into the CoFeP-CN composite filling most of the pores.

Figure S6 displays the high-resolution valence band X-ray photoelectron spectroscopy (XPS) spectrum of g-$C_3N_4$, CoFeP-CN, and $Li_2S$-CoFeP-CN samples. The intersection point of the linear fit of the valence band edge and the background determined the position of the valence band maximum (VBM).[27] The VBM of g-$C_3N_4$ was 1.87 eV above the Fermi level, confirming the semiconducting nature of g-$C_3N_4$.[38] In contrast, the VBM of CoFeP-CN was located 1.08 eV below the Fermi level, showing the metallic nature of the CoFeP-CN composite related to the metallic character of CoFeP.[39] Meanwhile, in line with the metallic nature of CoFeP-CN, the VBM of $Li_2S$-CoFeP-CN remained below the Fermi level while shifting to higher binding energies. The survey XPS spectrum shows the presence of Co, Fe, P, C, and N on the CoFeP-CN composite (Figure S7a).

Three bands can be fitted in the C 1s spectra of g-$C_3N_4$ and CoFeP-CN (Figure S7b), associated with C−C bonds, sp3 C (C−$NH_x$) and sp2-hybridized carbon in the aromatic ring (N−C=N), at 284.8 eV, 286.3 and 288.2 eV, respectively, for g-$C_3N_4$.[22,40] In CoFeP-CN, the N−C=N band appears slightly shifted towards higher binding energies, at 288.3 eV.[24] In $Li_2S$-CoFeP-CN, the O−C=O band appears at 289.8 eV indicating the presence of oxygen or oxygen-containing species on the surface of $Li_2S$.[41] In contrast, the N 1s spectrum experiences the opposite shift with the CoFeP introduction, as shown in Figure S7c. The three N 1s XPS peaks attributed to sp2-bonded N (C=N−C), N−$(C)_3$, and amino groups (N−$H_x$) are located at 399.17, 400.38, and 401.61 eV in g-$C_3N_4$, and negatively shift to 398.78, 400.32, and 401.41 eV in CoFeP-CN.[22,42] Notice that the pyridinic nitrogen, which effectively prevents the shuttle effect by the strong interaction of $Li^+$ in

polysulfides with N atoms,[12] accounts for about 70.6% of the total nitrogen. A new nitrogen chemical environment appears in $Li_2S$-CoFeP-CN, at 398.27 eV (Figure S7c). This is associated with a Li−N chemical interaction that has been reported to facilitate the $Li_2S$ decomposition.[43]

The complex Co 2p and Fe 2p XPS spectra of CoFeP-CN display at least two chemical states and several satellite peaks (Figure S7d,e). A doublet at 778.47 eV (Co $2p_{3/2}$) can be assigned to a Co−P chemical environment.[44] Additionally, as a result of the sample being exposed to air, a second doublet at higher binding energies is associated with a cobalt oxide or cobalt phosphate chemical environment.[24] Similarly, the Fe 2p spectrum displays a Fe−P component at 706.87 eV (Fe $2p_{3/2}$) and probably two oxide/phosphate components at 711.27 eV (Fe $2p_{3/2}$) and 714.47 eV (Fe $2p_{3/2}$) related to the partial oxidation of the sample during manipulation and transportation.[45] In the P 2p spectra of CoFeP-CN (Figure S7f), the doublet at 129.47 eV (P $2p_{3/2}$) is assigned P within a metal phosphide chemical environment and the doublet at 132.97 eV (P $2p_{3/2}$) is attributed to a phosphate environment related to the surface oxidation of the particles exposed to air.[46,47]

The Li 1s XPS spectrum of $Li_2S$-CoFeP-CN shows three closeby bands at 55.17, 55.32, and 55.87 eV (Figure S8a). The band at 55.17 eV is attributed to the Li−S bond within $Li_2S$.[8] The band at 55.87 is attributed to Li−N bonds involving electron transfer from the electron-rich pyridinic-N groups to Li.[48] The band at 55.32 eV can be assigned to a Li−OH environment generated during sample manipulation and transportation.[49]

The S 2p XPS spectrum of $Li_2S$-CoFeP-CN shows 4 doublets (Figure S8b). The doublet at 162.27 eV (S $2p_{3/2}$) is attributed to S within a $Li_2S$ chemical environment. The doublets at 166.97 eV (S $2p_{3/2}$) and 168.37 eV (S $2p_{3/2}$) are assigned to S−O ($SO_3$) and S−O ($SO_4$) chemical environments generated from the partial oxidation of the sample during manipulation and transportation before XPS measurements.[18,50] Finally, the doublet at 164.07 eV (S $2p_{3/2}$), which is

also observed in commercial $Li_2S$ may be attributed to $Li_2S$*−$SO_3$/$SO_4$.[41,51] Comparing the S 2p spectrum of $Li_2S$-CoFeP-CN with the reference $Li_2S$-KB-Co ($Li_2S$ grown on Ketjen black, KB, carbon loaded with cobalt, see Supporting Information for details) and $Li_2S$-CN ($Li_2S$ grown on g-$C_3N_4$, see Supporting Information for details) samples reveals that the introduction of CoFeP increases the $Li_2S$ component which can be attributed to terminal S−Co and S−Fe bonding.[46] Comparing the S 2p spectra of $Li_2S$-CN and $Li_2S$-CoFeP-CN shows that the peak associated with the Li−S bond shifts to lower binding energy in $Li_2S$-CoFeP-CN, which we hypothesize to be associated with electron transfer from Co and Fe atoms to S atoms in $Li_2S$.[46,52] This hypothesis is supported by the weakening of the relative intensity of the Co−O peak and the positive binding energy shift of the band corresponding to the Co−P environment in the Co 2p spectrum (Figure S8c). S−Co and S−Fe binding has been reported to facilitate the oxidation of $S^{2-}$ in $Li_2S$, thus lower activation voltage barriers are expected in $Li_2S$-CoFeP-CN electrodes.[53] Meanwhile, the presence of the sulfate components in all three S 2p spectra indicates a little oxidation of the samples' surfaces.

To determine the appropriateness of the sulfur host to improve the electrochemical performance of LSBs, its LiPS adsorption ability must be evaluated. In this direction, the polysulfide adsorption capability of CoFeP-CN was tested by suspending this material in a 10 mM $Li_2S_6$ solution (see details in the Supporting Information). After 12 hours at room temperature, we monitored the amount of $Li_2S_6$ remaining in the solution by visual inspection and using UV-vis spectroscopy, taking advantage of the absorbance band in the range 400-500 nm of $Li_2S_6$, which gives it an orange-brown color (Figure S9).[53] As a reference, the polysulfide adsorption capability of different samples was also analyzed by suspending them in the same solution. The color of the $Li_2S_6$ solution containing CoFeP-CN and CNT became significantly clearer than the reference samples

containing no absorber or carbon-based absorbers such as KB, KB-Co, and Super P, demonstrating the ability of g-$C_3N_4$ and CoFeP-CN to adsorb LiPSs. Adsorption results also confirmed that among the different samples, the CoFeP-CN composite has more active sites for adsorbing polysulfides.

Density functional theory (DFT) calculations were used to evaluate the interaction of CoFeP-CN with $Li_2S$ and determine the role of each element in its catalytic decomposition. g-$C_3N_4$ and metallic CoFeP with the CoFeP (112), and (020) facets were used to investigate the dissociation energy of $Li_2S$ (Figure S10). Figure 4a and S11 display the calculated $Li_2S$-CN and $Li_2S$-CoFeP molecular models. $Li_2S$ undergoes a stepwise delithiation process during charging, which we separate into two steps. The first step involves the delithiation of $Li_2S$ to a LiS cluster ($Li_2S \rightarrow LiS + Li^+ + e^-$), whereas the second one results in the complete separation of Li and S ($LiS \rightarrow S + Li^+ + e^-$). For steps 1/2, g-$C_3N_4$, CoFeP (112), and CoFeP (020) have associated dissociation barriers of 2.344/1.130, 0.547/0.215, and 0.238/0.306 eV, respectively (Figure 4b). Thus, the $Li_2S$ dissociation barriers on CoFeP surfaces are much lower than those of $Li_2S$ on g-$C_3N_4$, showing that CoFeP can efficiently promote the $Li_2S$ delithiation kinetics potentially increasing the utilization of active materials and decreasing the formation of dead $Li_2S$.[20,54]

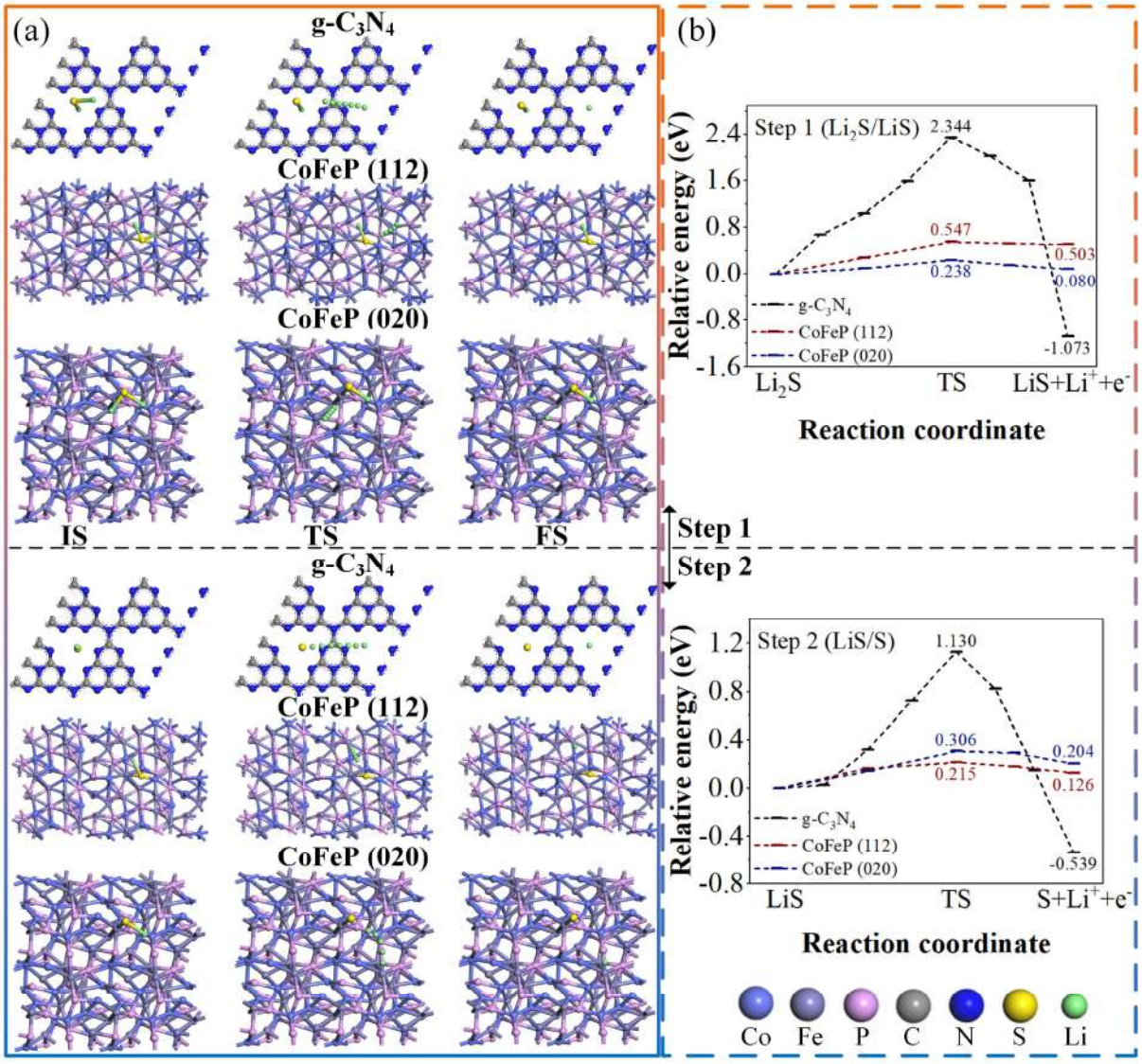


**Figure 4.** (a) Top view of DFT models and decomposition pathways of $Li_2S$ to sulfur on CNT, CoFeP (112), and CoFeP (020). (b) Energy profiles for the $Li_2S$ decomposition on CNT, CoFeP (112), and CoFeP (020). The initial state (IS), transition state (TS), and final state (FS), in that order, are each represented by its acronym.

According to DFT calculations, the Li−S bond length in $Li_2S$ is 2.28, 2.38, and 2.37 Å on g-$C_3N_4$, CoFeP (112), and CoFeP (020), respectively. These bond lengths are significantly longer than that of the single $Li_2S$ molecule (2.098 Å). This elongation of the Li−S bond points to an

easier decomposition of $Li_2S$ when bound at g-$C_3N_4$ or CoFeP surfaces. Besides, the Li−S bond on CoFeP is more stretched than on g-$C_3N_4$, thus resulting in a lower decomposition energy barrier. The adsorption energy of $Li_2S$ on g-$C_3N_4$ was calculated to be −1.78 eV and become more negative to −4.42 and −3.95 eV for CoFeP (020) and (112) surfaces. Thus the $Li_2S$ chemical interaction with CoFeP is stronger than with g-$C_3N_4$. Overall, DFT calculations show that the strong interaction between the N in g-$C_3N_4$ and Li in $Li_2S$, and between CoFeP and S in $Li_2S$ make the CoFeP-CN composite an appropriate $Li_2S$ host.[55]

To assess the electrochemical performances of $Li_2S$-CoFeP-CN composite in LSBs, coin-type half cells were assembled using a $Li_2S$-CoFeP-CN cathode and a pure Li-foil anode. As a reference, half cells with $Li_2S$-CN and $Li_2S$-KB-Co cathode materials were also assembled. As the electrolyte, a solution containing 1.0 M lithium bis(trifluoromethanesulfonyl)imide (LiTFSI), 1,2-dimethoxy ethane (DME), 1,3-dioxolane (DOL) (v/v = 1/1), and 0.2 M of $LiNO_3$ was used (see details in the Supporting Information). The electrochemical performance of the cathodes was initially tested using cyclic voltammetry (CV). Cathodes were swept between 1.7 V and 3.6 V (vs. $Li/Li^+$) at a scan rate of 0.1 mV $s^{-1}$ in the initial activation cycle, where an additional driving force is required to overcome the $Li_2S$ decomposition barrier (Figure 5a). After the activation cycle, cells were swept between 1.7 V and 2.8 V throughout the subsequent cycles.[1,56] In the first CV curve, a wide anodic peak (peak I) is measured at roughly 2.65 V in $Li_2S$-CoFeP-CN, 2.68 V for $Li_2S$-CN, and 3.54 V for $Li_2S$-KB-Co. This peak is related to the $Li_2S$ activation.[50] The $Li_2S$-CoFeP-CN and $Li_2S$-CN cathodes exhibit a smaller oxidation peak and activation voltage than $Li_2S$-KB-Co indicating that less energy is required for the initial activation of $Li_2S$ in these composites. This lower energy is related to the small and uniformly dispersed $Li_2S$ nanoparticles formed in carbon nitride and CoFeP-CN. It should be noted that the oxidation peak area of $Li_2S$-CoFeP-CN is larger

than that of $Li_2S$-CN. Since the surface of carbon nitride is not coated with CoFeP nanoparticles, nanoscale $Li_2S$ recrystallizes more uniformly than CoFeP-CN hosts during the synthesis, and the activation process in $Li_2S$-CN completes more quickly than in $Li_2S$-CoFeP-CN. After the initial charging, two reduction peaks (peak II and peak III in Figure 5a) are measured from the $Li_2S$-CoFeP-CN cathode at approximately 2.35 and 2.01 V. These peaks are attributed to the sequential reaction of sulfur with lithium ions to produce long-chain LiPSs ($Li_2S_x$, $4<x<8$) and the subsequent formation of insoluble $Li_2S$ and $Li_2S_2$.[8] These results indicate that among the tested materials, CoFeP-CN was the most effective in activating the $Li_2S$ and promoting the polysulfides redox reactions kinetics.

To compare the catalytic activity of the host materials, the onset potential, defined as the voltage required for the current density to exceed the baseline current by 10 mA $g^{-1}$, was determined and plotted (Figure S12).[57] $Li_2S$-CoFeP-CN displays the lowest onset potentials for oxidation peaks and the highest for reduction peaks among the three types of electrodes tested (Figure 5b), demonstrating a successful reduction of the overpotential in LiPS conversion reaction.

After the initial activation cycle, the CV profiles show the characteristic sulfur cathode features (Figure S13a), including a broad anodic peak associated with the conversion of $Li_2S_2$ and $Li_2S$ into polysulfides and $S_8$ (peak I) and two cathodic peaks (peak II and III) corresponding to the two-step S reduction process.[58] Although the $Li_2S$-CN shows the highest oxidation peak current density during initial activation, the $Li_2S$-CoFeP-CN composite displays the highest oxidation peak current density after activation. This result indicates that, at the end of the first discharge process, $Li_2S$ nanoparticles can recrystallize with a smaller size and more uniformly in $Li_2S$-CoFeP-CN than in the $Li_2S$-CN due to the catalytic role of CoFeP nanocrystals. Furthermore, the peak and onset potentials are displayed in Figure S13b. Among the tested samples, the $Li_2S$-CoFeP-CN cathode

was characterized by the lowest oxidation potentials and the highest reduction peaks, indicating the lowest polarization and best reversibility.

CV measurements at various scan rates of 0.1 to 0.5 mV $s^{-1}$ examined the kinetics of lithium-ion insertion/extraction at the $Li_2S$-CoFeP-CN interface and the lithium-ion diffusion rate in the cell (Figure 5c). The CV curves of the $Li_2S$-CoFeP-CN cathode exhibit good repeatability throughout subsequent cycles in terms of peak position and curve shape, indicating high reversibility of the multistep redox processes. The polarization voltage slowly increased as a result of the anodic peak shifting to a positive potential and the two cathodic peaks shifting to more negative potentials when the scan rate increased. The Li-ion diffusivity of different hosts was investigated using the classical Randles−Sevcik equation:[41]

$$I_P=2.69\times10^5 n^{3/2} A D_{Li^+}^{1/2} v^{1/2} C_{Li^+} \quad (1)$$

where $I_p$ indicates the peak current, n is the number of charge transfers, A is the electrode area, D is the $Li^+$ diffusion coefficient, $v$ is the scan rate, and $C_{Li^+}$ is the Li-ion concentration in the electrolyte. The Li-ion mobility in cathodes with constant n, A, and $C_{Li^+}$ is reflected in the slope of the linear fit between the peak currents and the square root of the scanning rates (Figure S14). The Li-ion diffusion coefficient can be estimated through a linear fitting of $I_p$ vs. $v^{1/2}$, with $k = I_p/v^{1/2}$.[41] The $Li_2S$-CoFeP-CN electrode exhibits larger slopes ($k_1$ = 141, $k_2$ = 59.2, and $k_3$ = 53.2) than $Li_2S$-KB-Co ($k_1$ = 28.7, $k_2$ = 40.4, and $k_3$ = 41.7) electrodes (Figure 5d). The much higher slopes measured for the $Li_2S$-CoFeP-CN cathode during both charge and discharge processes indicate that the CoFeP-CN host greatly facilitates the $Li^+$ diffusion, enhancing the polysulfide conversion kinetics throughout the entire $Li^+$ insertion/extraction processes.[8,41,54]

Figure 5e displays the initial charging profiles of the different electrodes. During the first charging phase, the $Li_2S$ converts to sulfur which requires a significant overpotential that may

damage the ether-based electrolyte (Figure S15a). At the same time, the lower the overpotential for the $Li_2S$ oxidation, the higher the depth of charge that can be obtained during the first and subsequent cycles. Thus, the first activation of $Li_2S$-based batteries is crucial to their posterior electrochemical performance.[59] The $Li_2S$-CoFeP-CN charging curve has a smaller peak and lower charging plateau, which suggests that the CoFeP-CN composite promotes $Li_2S$ activation. A slight electrolyte decomposition when the cell is charged up to 3.6 V may cause the initial charge capacity to exceed the theoretical value.[60] Compared with previous works activating the $Li_2S$ cathodes at 0.1 C in the initial cycle, the $Li_2S$-CoFeP-CN cathode demonstrates an outstandingly low charge overpotential (Figure S15a). This result is related both to the small size of the initial $Li_2S$ particles and the excellent electrocatalytic properties of CoFeP-CN.

Following the first cycle at a current rate of 0.1 C (1 C = 1166 mA $g^{-1}$), the charging-discharging tests for the three different types of electrodes are shown in Figure 5f. Consistently with CV curves, all electrodes displayed one plateau during charging and two plateaus during discharging. $Li_2S$-CoFeP-CN provided substantially longer charging and discharging plateaus than other cathodes. The $Li_2S$-CoFeP-CN cathode also displayed a lower polarization value ($\Delta E$ = 177 mV) compared with $Li_2S$-KB-Co ($\Delta E$ = 195 mV), and $Li_2S$-CN ($\Delta E$ = 252 mV) electrodes (Figure 5g). Besides, the $Li_2S$-CoFeP-CN electrode showed the lowest overpotentials throughout the charging process (inset of Figure 5f).[60] The capacity resulting from the conversion of sulfur to $Li_2S_4$ in the first discharge plateau is generally named $Q_1$, and the capacity resulting from the conversion of $Li_2S_4$ into $Li_2S_2$/$Li_2S$ in the second discharge plateau is $Q_2$ (Figure 5f). The higher $Q_2/Q_1$ ratio, the better the catalytic ability of the host material since a large $Q_2$ indicates minimized loss of LiPS during the process and closer reach to the reaction completion.[24] The $Li_2S$-CoFeP-CN cathode showed

the highest $Q_2/Q_1$ ratio at 2.83, demonstrating a superior catalytic effect of CoFeP-CN for the sluggish LiPS redox reaction kinetics (Figure 5g).

To better understand the improved reaction kinetics of $Li_2S$-CoFeP-CN and establish the relationship between cycling performance and electrode kinetics, electrochemical impedance spectroscopy (EIS) measurements on fresh cells in an open circuit (Figure 5h), as well as CV and EIS measurements on cycled $Li_2S$-CoFeP-CN cells (Figure 5i) were performed. In the high-medium frequency zone, one depressed semicircle was observed on each of the Nyquist plots of the three batteries, whereas at the low frequency, a sloped line was measured. EIS data were fitted using the equivalent circuit shown in the inset of Figure 5h, where $R_e$ is the bulk electrolyte resistance, $R_{sf}$ is the surface film resistance, $R_{ct}$ is the charge-transfer resistance, $CPE_{(sf+dl)}$ is a constant phase element, $Z_w$ is the Warburg impedance, and $C_{int}$ is an intercalation capacitance describing the accumulation of lithium at the very low-frequency range.[61-63] Both, $Li_2S$-CoFeP-CN and $Li_2S$-KB-Co-based cells exhibited similarly low $R_e$ values, proving that the cells were correctly manufactured and assembled under identical conditions (Table S2). For all the materials, $R_e$ increased upon cycling, which is related to an increase in the electrolyte viscosity associated with the dissolution of the polysulfides. However, notice that even after 200 cycles, the $Li_2S$-CoFeP-CN cathode displayed a small and stable $R_e$, indicating that the CoFeP-CN host can effectively contain most of the generated LiPSs.[54] A single semicircle is observed in the high-medium frequency, which is considered as the combination of the surface film and charge-transfer resistance.[62] $R_{(sf+ct)}$ is much lower for the $Li_2S$-CoFeP-CN than for $Li_2S$-KB-Co, which confirms the faster Li-ion diffusion and charge-transfer process within the former. The large semicircle at the beginning of the charging process reveals a substantial interphase contact resistance $R_{sf}$ caused by the electrically insulating nature of $Li_2S$. After cycling, a smaller semicircle is observed in the

high-medium frequency, indicating the formation of soluble polysulfides that facilitate the charge transfer on the $Li_2S$ surface and improve interphase electronic interaction between the particles (inset of Figure 5i).[1,64] Besides, before cycling, a large low-frequency tail slope was measured for all the samples. The linear tail in the low-frequency region (<1 Hz) is associated with the Li-ion diffusion impedance. The slope of the tail at the lowest frequency is discovered to tilt away from 45º, which is characterized by an intercalation capacitance in the equivalent circuit.[63,65,66] For fresh cells, due to the blocking character of the electrodes resulting from the low conductivity of the high amount of $Li_2S$ that coated the hosts, the tail is more capacitive and Warburg impedance has a lower contribution. After cycling, a decrease in the slope of the low-frequency tail is attributed to a decrease in the capacitive impedance contribution and an approach to Warburg diffusion behavior. Meanwhile, the shorter low-frequency tail indicates the better redistribution of $Li_2S$ species over the CoFeP-CN host during cycling without creating excessive Li-ion diffusional resistance, resulting in faster Li-ion diffusion in the electrode.[59,67] Overall, CV and EIS data indicate that the $Li_2S$-CoFeP-CN electrode is characterized by excellent electrical conductivity and electrode kinetics.

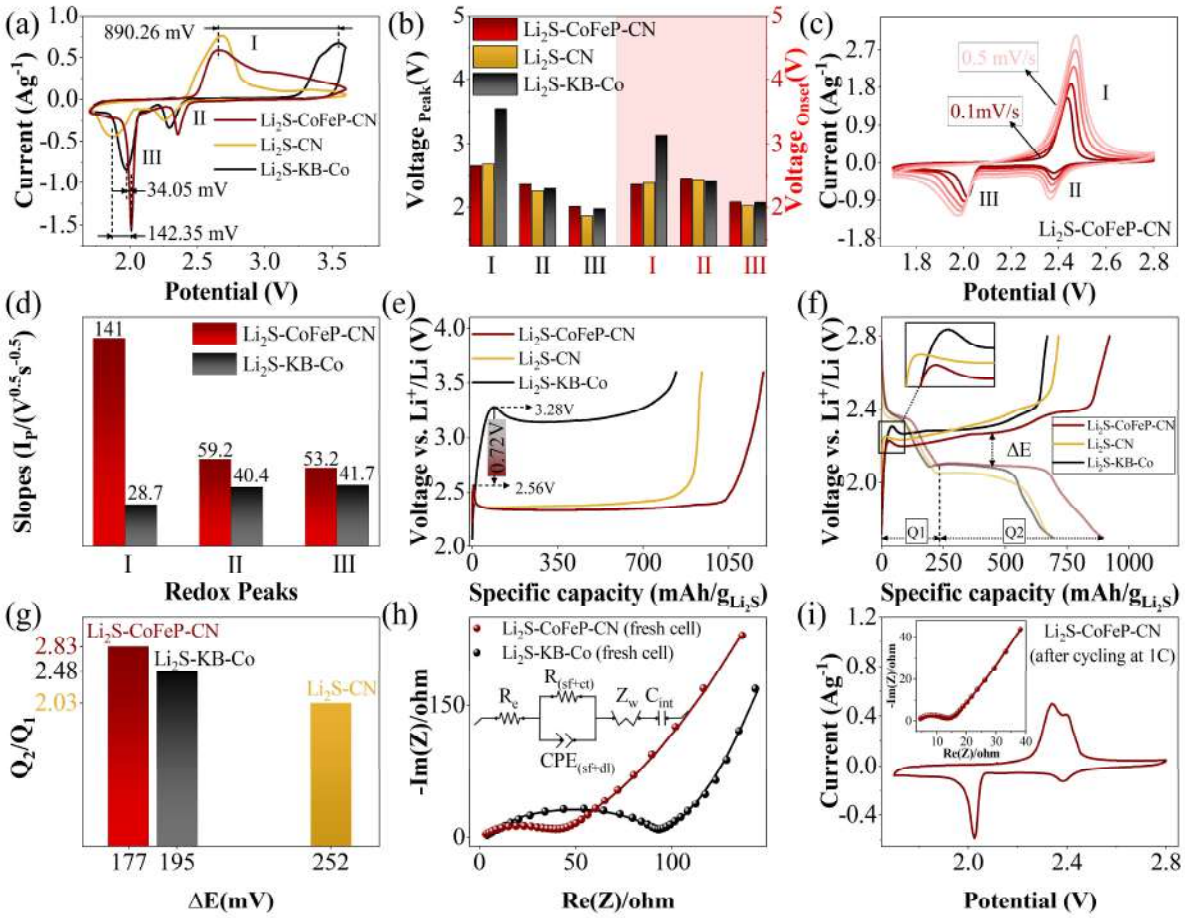


**Figure 5.** (a) Initial CV curves of $Li_2S$-CoFeP-CN, $Li_2S$-CN, and $Li_2S$-KB-Co electrodes at a scanning rate of 0.1 mV $s^{-1}$ between 1.7 and 3.6 V. (b) Peak voltages and onset potentials from initial CV curves of different electrodes. (c) CV curves of $Li_2S$-CoFeP-CN electrode at different scan rates. (d) The $I_p/v^{1/2}$ values obtained from CV curves of $Li_2S$-CoFeP-CN. (e) Initial charging profiles of different electrodes at a current rate of 0.1 C. (f) Charging-discharging profiles of different electrodes at the current rate of 0.1 C after the initial activation cycle. (g) ΔE and $Q_2/Q_1$ values obtained from charging-discharging profiles of different electrodes after the initial cycle. (h) EIS plot of $Li_2S$-CoFeP-CN and $Li_2S$-KB-Co electrodes before cycling. The equivalent circuit is shown as an inset. (i) CV and EIS measurements for $Li_2S$-CoFeP-CN electrode after cycling at 1 C.

The rate capability of the as-prepared cathodes was assessed by cycling the cells at C-rates between 0.1C and 5C (Figure 6a,b). Figure S15b shows the initial galvanostatic charge-discharge (GCD) curve in the voltage window 1.7−3.6 V of the $Li_2S$-CoFeP-CN cathode at 0.1 C. $Li_2S$-CoFeP-CN has an outstanding initial discharging capacity of 991 mAh $g_{Li_2S}^{-1}$, i.e. 1420 mAh $g_S^{-1}$, compared with reported data (Table S3). This large initial capacity demonstrates a high utilization of $Li_2S$ active species. After the initial cycle, cathodes are cycled between 1.7 and 2.8 V and investigated at various C-rates following the initial activation cycle (Figure 6a). When increasing the current rate, the polarization of the charge and discharge increased gradually, especially at a low current rate range. Even at a high current density of 5C, all discharge curves showed two long and flat discharge plateaus. As shown in Figure 6b, $Li_2S$-CoFeP-CN delivered an initial discharging capacity of 991 mAh $g^{-1}$ at 0.1C, well above that of $Li_2S$-CN at 770 mAh $g^{-1}$ and $Li_2S$-KB-Co at 830 mAh $g^{-1}$. The average discharge capacity of $Li_2S$-CoFeP-CN for 0.1, 0.2, 0.5, 1, 2, and 5C was 874, 741, 660, 610, 541, and 458 mAh $g^{-1}$, respectively, which are markedly higher than those of the $Li_2S$-CN and $Li_2S$-KB-Co cathodes. When the discharge current density returned to 0.2C after running at high current densities, a high discharge capacity of 727 mAh $g^{-1}$ was still recovered, demonstrating a good rate capability and stability.

To assess the cycling performance, half cells were first charged from the open-circuit voltage (OCV) to 3.6 V at 0.1 C for 1 cycle to activate the $Li_2S$. Thereafter, the cycling performance of the different host materials was investigated at 0.2C between 1.7 and 2.8 V (Figure 6c). The $Li_2S$-CoFeP-CN battery delivered a discharge specific capacity of 756 mAh $g^{-1}$ at the first cycle after initial activation and maintained 641 mAh $g^{-1}$ after 150 cycles, thus showing a low capacity fading rate of 0.1% per cycle. In contrast, the initial capacity of $Li_2S$-KB-Co was 524 mAh $g^{-1}$ and showed a 0.21% capacity fade per cycle.

When the current density was increased to 1C after activation at 0.1C, a discharge specific capacity of 619 and 395 mAh $g^{-1}$ was obtained for $Li_2S$-CoFeP-CN and $Li_2S$-KB-Co, respectively (Figure 6d). During long-term cycling tests at 1C, the $Li_2S$-CoFeP-CN cathodes exhibit higher specific capacity and stable capacity retention of 97% and 88% after 100 and 400 cycles, respectively, corresponding to a small fading rate of 0.029% per cycle. In contrast, the $Li_2S$-KB-Co electrode exhibits faster capacity fading and poor cycling performance with a higher fading rate of 0.098 after 400 cycles. The Coulombic efficiencies of $Li_2S$-CoFeP-CN at 1 C reach above 99.5% after the first cycle and remain close to 100% even after 800 cycles. The Coulombic efficiencies of $Li_2S$-KB-Co are lower than those of $Li_2S$-CoFeP-CN accounting for the poorer LiPS trapping at KB-Co and the related increase in electrolyte degradation.

A comparison of the electrochemical performances of $Li_2S$ cathodes reported in the literature is included in Table S3. $Li_2S$-CoFeP-CN is among the best $Li_2S$ cathodes reported in terms of activation barrier, initial discharge capacity, rate capability, and cycle life.

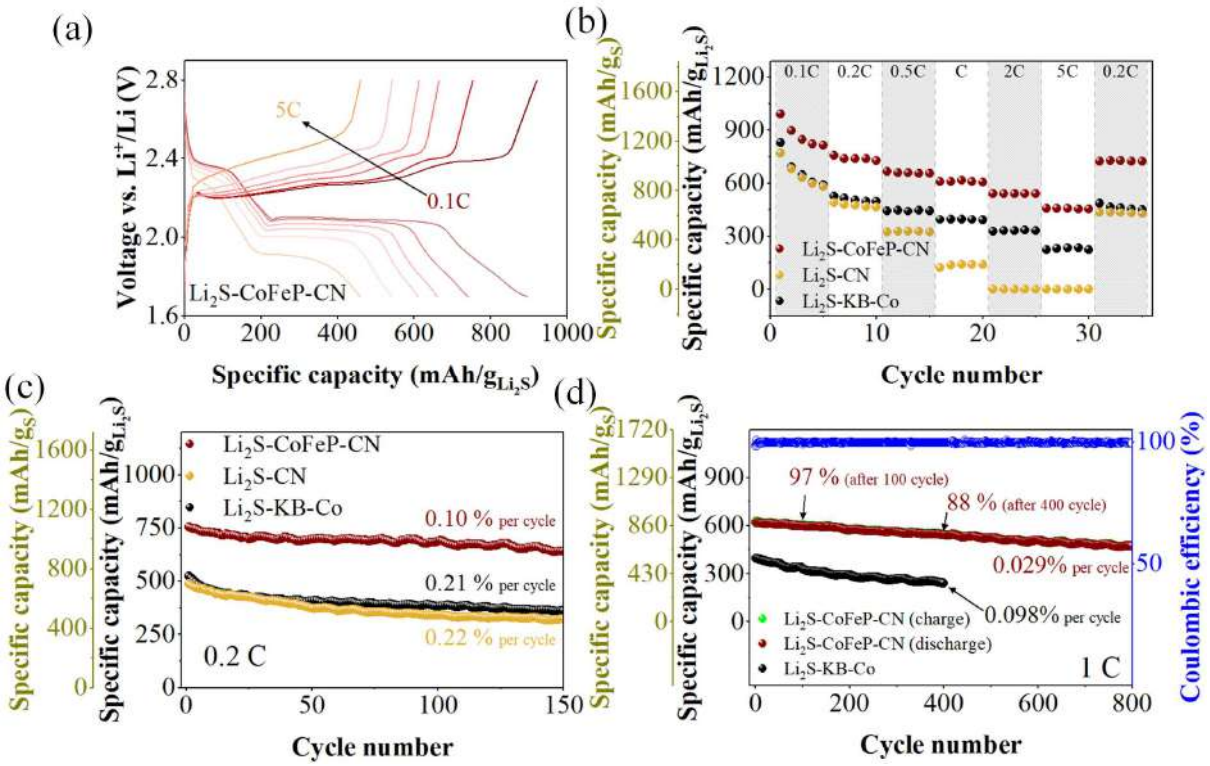


**Figure 6.** (a) Charging-discharging profiles of $Li_2S$-CoFeP-CN electrode at different current rates. (b) C-rate performances of $Li_2S$-CoFeP-CN, $Li_2S$-CN, and $Li_2S$-KB-Co. (c) Cycling performances at 0.2C for different electrodes. (d) Long-term cycling stability and Coulombic efficiencies of $Li_2S$-CoFeP-CN electrode compare with cycling stability of $Li_2S$-KB-Co electrode at 1 C.

To evaluate the capability of the $Li_2S$-CoFeP-CN cathode in pairing with safer anodes other than Li, here, $Li_2S$-CoFeP-CN cathodes were further coupled with a silicon-based anode made of silicon nanowires (NWs) grown on graphite particles (Gt-SiNW).[68,69] Silicon, with its high theoretical capacity and low environmental impact, is regarded as one of the most attractive alternative anodes for lithium metal in LSBs. However, silicon experiences a significant volume change during lithiation and a low electrical conductivity. To overcome these limitations, the distribution of SiNWs on graphite in the Gt-SiNW composite accommodates huge volume fluctuations during cycling and avoids electrode pulverization. Additionally, the strong connection of SiNWs to the

graphite surface provides improved charge transport properties.[68] Figure S16 shows SEM images of the Gt-SiNW composite. The Si content in Gt-SiNW is around 25 wt.% (Table S4).

Before assembling the full cell, the Gt-SiNW anode was tested with carbonate- and ether-based electrolytes (see details in the Supporting Information, Figure S17a). Using a carbonate electrolyte, in the cathodic scan the sharp peak below 0.1 V corresponds to the lithiation of crystalline silicon and graphite, whereas in the ether electrolyte, in addition to the peak below 0.1 V, two minor peaks around 1.51 and 0.53 V could be related to the reduction of $LiNO_3$ and formation of SEI layers, respectively.[70] The delithiation of $Li_xC_6$ and the Li−Si alloy is reflected by peaks in the anodic scan with carbonate electrolyte at 0.16 and 0.45 V. In contrast, in the ether electrolyte, the first peak associated with the delithiation of graphite has nearly vanished, leaving only the peak associated with the delithiation of the Li−Si alloy visible, which also demonstrates the formation of the SEI layer during the first cycle of the Gt-SiNW in the ether-based electrolyte. Further pieces of evidence of the partial decomposition of the electrolyte and the formation of the SEI layer are provided by the plateau at 0.6 V in the initial discharge curve of the Gt-SiNW anode with the ether-based electrolyte (Figure S17b). The Gt-SiNW half cells were first discharged at constant current constant voltage (CCCV), at 0.05C to 0.01 V, and then the voltage was held at 0.01 V while the current decreased to 0.01C. The half cell charge-discharge protocol is detailed in Table S5. Figure S17c shows the C-rate performance comparison of Gt-SiNW in carbonate and ether electrolytes at a relatively high anode active material loading of 3.3 $\mathrm{mg\,cm^{-2}}$. The Gt-SiNW anode shows an initial specific capacity of 1714 mAh $g^{-1}$ in carbonate electrolyte and 1511 mAh $g^{-1}$ in ether electrolyte. Therefore, different electrolytes have dissimilar impact on the performance of the Gt-SiNW anode. As previously reported, the type of electrolyte and additives employed can affect the properties of the SEI formed on silicon-based anodes, making them extremely sensitive to the

electrolyte. On the other hand, due to the large volume change of silicon anodes during cycling, the formed SEI has a major impact on their performance. In ether-based electrolytes, unstable SEI and irreversible electrolyte decomposition lead to higher capacity fading and lower Coulombic efficiency in silicon anodes.[70] Figure S17d shows the cycling performance of Gt-SiNW electrode at 0.1C in the ether-based electrolyte. The high initial discharge capacity and low average discharge voltage (around 0.3 V vs $Li/Li^+$) of the Gt-SiNW anode make it suitable to pair with the $Li_2S$-CoFeP-CN cathode.

A scheme of the $Li_2S$-CoFeP-CN/Gt-SiNW full cell is depicted in Figure 7a. The electrode reactions are based on the assumption that the cell has a theoretical 4.4Li-storage anode and 2Li-storage cathode. The Gt-SiNW anode was lithiated for one cycle at 0.05C before assembling in full cell configuration. Tables S5 and S6 provide information on the prelithiation approach and anode balancing. The carbonate-based electrolyte provides the best performance in Si-based anodes, but in sulfur-based cathodes, the irreversible chemical reaction between nucleophilic $Li_2S_x$ intermediates and electrophilic carbonate-based solvents causes rapid capacity fading due to loss of sulfur.[13] Due to the poor performance of $Li_2S$-CoFeP-CN cathode with carbonate electrolyte, the full cells were cycled using the same ether electrolyte used in the half cell test of $Li_2S$-CoFeP-CN. The GCD curves of full cells were cycled between 1.5 and 3.6 V at 0.1C for the first cycle and 1.5 to 2.8 V for the following cycles (Figure 7b). The initial GCD curve of the prelithiated full cell exhibits one charge plateau with an activation barrier of around 3 V and two discharge plateaus, similar to the sulfur half cells. The charging activation barrier disappears in the second cycle after activation. In the activation cycle, the full cell exhibits a high discharge capacity of 903 mAh $g_{Li_2S}^{-1}$. Figure 7b depicts the GCD curve of the full cell at 0.2C after a first activation cycle at 0.1C. The charge-discharge plateaus at 0.2C are comparable with GCD curves at 0.1C but the

plateaus become slopping. At 0.1C, after the first initial activation, the full cell delivered a discharge capacity of 805.6 mAh $g_{Li_2S}^{-1}$ and maintained 519 mAh $g_{Li_2S}^{-1}$ after 80 cycles (Figure 7c). The Coulombic efficiency was 71.9% during the activation cycle at 0.1C, raised to 89.7% during the second cycle, and reached 96.3% on average during the following cycles. Compared to $Li_2S$ half cells, the full cell exhibits a poorer Coulombic efficiency and a faster capacity loss. During the discharge process of half cell test, the lithium foil counter electrodes in half cells can supply enough lithium ions, but in full cells, both electrodes participate in capacity loss. The higher capacity fading of the Si/$Li_2S$ full cell is also attributed to the unfavorable SEI layer formation at the anode using the ether-based electrolyte.[70] At 0.2 C, the full cell delivers a discharge capacity of 560.7 mAh $g_{Li_2S}^{-1}$ after activation and shows a capacity fading rate of 0.28% per cycle after 150 cycles (Figure 7d).

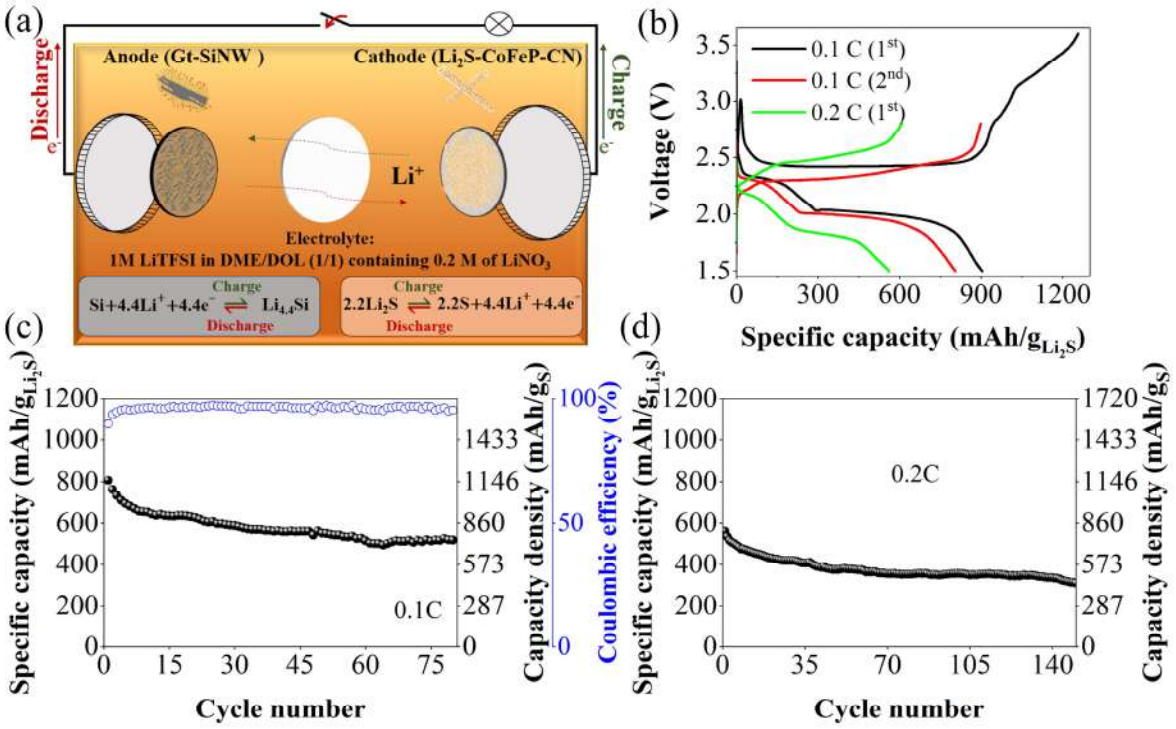

**Figure 7.** Electrochemical performances of Gt-SiNW/$Li_2S$-CoFeP-CN full cell (a) Schematic of full cell components. (b) Charging-discharging curves of a full cell at different current rates. (c and d). Cycling performances of a full cell at (c) 0.1 C, (d) 0.2 C.

Gt-SiNW/$Li_2S$-CoFeP-CN full cell displays a shorter cycle life than half cells due to issues originating from both the cathode and anode. The primary cause of the reduced cycle life, aside from the polysulfide shuttle effect, is the impact of ether-based electrolytes on the SEI formation of the Gt-SiNW anode. The performance of silicon-carbon-based anodes was mostly investigated in carbonate electrolytes, and the challenging impact of ether electrolytes on silicon-carbon-based anode performance has not been comprehensively studied. Therefore, to efficiently improve the electrochemical performance of the Si/$Li_2S$ full cell, in addition to reducing the polysulfide shuttle effect of the $Li_2S$ cathodes, a more stable SEI formation on the silicon-carbon-based anodes should be achieved by addressing the issues associated with the use of ether-based electrolytes.

## Conclusion

In summary, a nanostructured $Li_2S$-CoFeP-CN composite was proposed as an effective cathode in LSBs. CoFeP-CN was produced using a facile one-pot heating-up reaction based on the growth of the bimetallic phosphide CoFeP nanocrystals on the surface of the tubular g-$C_3N_4$. CoFeP-CN displays excellent electrical conductivity and LiPSs adsorption properties. A liquid infiltration-evaporation method was used to grow $Li_2S$ nanocrystals and generate the $Li_2S$-CoFeP-CN nanocomposite. Along with CoFeP, which has abundant adsorption sites and metallic properties, the mesoporous structure and high pyridinic nitrogen content of tubular carbon nitride that acts as a backbone helps to accommodate volume change, promotes Li ion diffusion and strongly suppresses polysulfides shuttle. The small size of the $Li_2S$ particles facilitates their activation and physical confinement, as well as buffering the sulfur volume changes, enabling high cathode

performance. DFT calculations and experimental results show that both g-$C_3N_4$ and CoFeP not only have a strong ability to weaken the Li−S bonds and reduce the activation barrier by strong Li−N and metal-sulfur bonds but also have high $Li_2S$ adsorption capability. Paired with the advantages of the CoFeP-CN, the $Li_2S$-CoFeP-CN composite displays a high content of $Li_2S$ (67 wt.%), a low activation barrier, a high initial capacity of 991 mAh $g_{Li_2S}^{-1}$ (close to 85% of the theoretical capacity of $Li_2S$), and excellent rate capability up to 5 C. This study also examined the performance of $Li_2S$-KB-Co and $Li_2S$-CN, and the results indicated that $Li_2S$-CoFeP-CN has superior electrochemical reaction kinetics to the latter two. To further investigate the electrochemical performance of the $Li_2S$-CoFeP-CN electrode, a full cell with $Li_2S$-CoFeP-CN cathode and prelithiated Gt-SiNW anode was also assembled. The full cell exhibits high initial discharge capacity and relatively good cycling stability in an ether electrolyte. Nevertheless, to increase the cyclability of the full cell, it is necessary to minimize ether electrolyte depletion during the cycling. In this direction, further research has to be done to evaluate the effect of various additives in ether-based electrolytes on different structures of silicon-carbon-based anodes.

## Supporting Information

Experimental details, calculation details, additional electron microscopy data, XRD fitting results, $N_2$ adsorption-desorption isotherms, XPS data, UV-vis data, additional results from DFT calculation and from the electrochemical characterization of the materials and devices, tables detailing and comparing the material's and device's parameters.

## Author Information


### Corresponding Authors

***E-mail:** acabot@irec.cat

***E-mail:** m.oloomi@um.ac.ir

***E-mail:** xqqi@cqut.edu.cn

**Author Contributions**

Hamid Mollania: conceptualization, methodology, investigation (lead), formal analysis (lead), visualization, data curation, writing – original draft. Chaoqi Zhang: investigation (supporting). Ruifeng Du: investigation (supporting), methodology. Xueqiang Qi: formal analysis (supporting). Junshan Li: investigation (supporting). Sharona Horta: investigation (supporting). Maria Ibañez: investigation (supporting). Caroline Keller: investigation in the synthesis of Gt-SiNWs material. Pascale Chenevier: supervision, resources, investigation in the synthesis of Gt-SiNWs material. Majid Oloomi-Buygi: supervision, writing – review & editing. Andreu Cabot: project administration, supervision, funding acquisition, resources, conceptualization, methodology, writing – review & editing. All authors have read and agreed to the published version of the manuscript. All the images/artwork/photos that appear in the manuscript and Supporting Information, including those in the TOC graphic, were created by the authors of this study.

## Conflict of Interest

The authors declare no conflict of interest.

## Acknowledgements

The authors acknowledge support from the 2BoSS project of the ERA-MIN3 program with the Spanish grant number PCI2022-132985/AEI/10.13039/501100011033 and the French grant number ANR-22-MIN3-0003-01. J.L. acknowledges support from the Natural Science Foundation of Sichuan Province 2022NSFSC1229. The authors acknowledge funding from Generalitat de Catalunya 2021 SGR 01581 and European Union NextGenerationEU/PRTR.

## References

(1) Ye, H.; Li, M.; Liu, T.; Li, Y.; Lu, J. Activating $Li_2S$ as the Lithium-Containing Cathode in Lithium–Sulfur Batteries. *ACS Energy Lett.* **2020**, *5* (7), 2234-2245. DOI: 10.1021/acsenergylett.0c00936.

(2) Xiang, J.; Zhao, Y.; Wang, L.; Zha, C. The Presolvation Strategy of $Li_2S$ Cathodes for Lithium–Sulfur Batteries: A Review. *J. Mater. Chem. A* **2022**, *10* (19), 10326-10341. DOI: 10.1039/d2ta01008a.

(3) Jiang, J.; Fan, Q.; Chou, S.; Guo, Z.; Konstantinov, K.; Liu, H.; Wang, J. $Li_2S$-Based Li-Ion Sulfur Batteries: Progress and Prospects. *Small* **2021**, *17* (9), e1903934. DOI: 10.1002/smll.201903934 From NLM PubMed-not-MEDLINE.

(4) Yang, D.; Liang, Z.; Tang, P.; Zhang, C.; Tang, M.; Li, Q.; Biendicho, J. J.; Li, J.; Heggen, M.; Dunin-Borkowski, R. E.; Xu, M.; Llorca, J.; Arbiol, J.; Morante, J. R.; Chou, S. L.; Cabot, A. A High Conductivity 1D π-d Conjugated Metal-Organic Framework with Efficient Polysulfide Trapping-Diffusion-Catalysis in Lithium-Sulfur Batteries. *Adv. Mater.* **2022**, *34* (10), e2108835. DOI: 10.1002/adma.202108835 From NLM PubMed-not-MEDLINE.

(5) Yang, D.; Li, M.; Zheng, X.; Han, X.; Zhang, C.; Jacas Biendicho, J.; Llorca, J.; Wang, J.; Hao, H.; Li, J.; Henkelman, G.; Arbiol, J.; Morante, J. R.; Mitlin, D.; Chou, S.; Cabot, A. Phase Engineering of Defective Copper Selenide toward Robust Lithium-Sulfur Batteries. *ACS Nano* **2022**, *16* (7), 11102-11114. DOI: 10.1021/acsnano.2c03788 From NLM PubMed-not-MEDLINE.

(6) Zhang, C.; Fei, B.; Yang, D.; Zhan, H.; Wang, J.; Diao, J.; Li, J.; Henkelman, G.; Cai, D.; Biendicho, J. J.; Morante, J. R.; Cabot, A. Robust Lithium–Sulfur Batteries Enabled by Highly Conductive $WSe_2$-Based Superlattices with Tunable Interlayer Space. *Adv. Funct. Mater.* **2022**, *32* (24). DOI: 10.1002/adfm.202201322.

(7) Li, M.; Yang, D.; Biendicho, J. J.; Han, X.; Zhang, C.; Liu, K.; Diao, J.; Li, J.; Wang, J.; Heggen, M.; Dunin-Borkowski, R. E.; Wang, J.; Henkelman, G.; Morante, J. R.; Arbiol, J.; Chou, S. L.; Cabot, A. Enhanced Polysulfide Conversion with Highly Conductive and Electrocatalytic Iodine-Doped Bismuth Selenide Nanosheets in Lithium–Sulfur Batteries. *Adv. Funct. Mater.* **2022**, *32* (26). DOI: 10.1002/adfm.202200529.

(8) Yu, M.; Zhou, S.; Wang, Z.; Pei, W.; Liu, X.; Liu, C.; Yan, C.; Meng, X.; Wang, S.; Zhao, J.; Qiu, J. A Molecular-Cage Strategy Enabling Efficient Chemisorption–Electrocatalytic Interface in Nanostructured $Li_2S$ Cathode for Li Metal-Free Rechargeable Cells with High Energy. *Adv. Funct. Mater.* **2019**, *29* (46). DOI: 10.1002/adfm.201905986.

(9) Hao, Z.; Chen, J.; Yuan, L.; Bing, Q.; Liu, J.; Chen, W.; Li, Z.; Wang, F. R.; Huang, Y. Advanced $Li_2S$/Si Full Battery Enabled by Tin Polysulfide Immobilizer. *Small* **2019**, *15* (50), e1902377. DOI: 10.1002/smll.201902377 From NLM PubMed-not-MEDLINE.

(10) Liu, M.; Ren, Y. X.; Jiang, H. R.; Luo, C.; Kang, F. Y.; Zhao, T. S. An Efficient $Li_2S$-Based Lithium-Ion Sulfur Battery Realized by a Bifunctional Electrolyte Additive. *Nano Energy* **2017**, *40*, 240-247. DOI: 10.1016/j.nanoen.2017.08.017.

(11) Yu, M.; Wang, Z.; Wang, Y.; Dong, Y.; Qiu, J. Freestanding Flexible $Li_2S$ Paper Electrode with High Mass and Capacity Loading for High-Energy Li-S Batteries. *Adv. Energy Mater.* **2017**, *7* (17). DOI: 10.1002/aenm.201700018.

(12) Yu, H.; Zeng, P.; Zhou, X.; Guo, C.; Liu, X.; Wang, K.; Guo, X.; Chang, B.; Chen, M.; Wang, X. Atomically Dispersed and O, N-Coordinated Mn-Based Catalyst for Promoting the Conversion of Polysulfides in $Li_2S$-Based Li-S Battery. *ACS Appl. Mater. Interfaces* **2021**, *13* (45), 54113-54123. DOI: 10.1021/acsami.1c18645 From NLM PubMed-not-MEDLINE.

(13) Li, S.; Leng, D.; Li, W.; Qie, L.; Dong, Z.; Cheng, Z.; Fan, Z. Recent Progress in Developing $Li_2S$ Cathodes for Li–S Batteries. *Energy Storage Mater.* **2020**, *27*, 279-296. DOI: 10.1016/j.ensm.2020.02.010.

(14) Wang, Z.; Xu, C.; Chen, L.; Si, J.; Li, W.; Huang, S.; Jiang, Y.; Chen, Z.; Zhao, B. In-Situ Lithiation Synthesis of Nano-Sized Lithium Sulfide/Graphene Aerogel with Covalent Bond Interaction for Inhibiting the Polysulfides Shuttle of Li-S Batteries. *Electrochim. Acta* **2019**, *312*, 282-290. DOI: 10.1016/j.electacta.2019.04.169.

(15) Yuan, K.; Yuan, L.; Chen, J.; Xiang, J.; Liao, Y.; Li, Z.; Huang, Y. Methods and Cost Estimation for the Synthesis of Nanosized Lithium Sulfide. *Small Struct.* **2020**, *2* (3). DOI: 10.1002/sstr.202000059.

(16) Wu, F.; Pollard, T. P.; Zhao, E.; Xiao, Y.; Olguin, M.; Borodin, O.; Yushin, G. Layered $LiTiO_2$ for the Protection of $Li_2S$ Cathodes against Dissolution: Mechanisms of the Remarkable Performance Boost. *Energy Environ. Sci.* **2018**, *11* (4), 807-817. DOI: 10.1039/c8ee00419f.

(17) Zheng, S.; Chen, Y.; Xu, Y.; Yi, F.; Zhu, Y.; Liu, Y.; Yang, J.; Wang, C. In Situ Formed Lithium Sulfide/Microporous Carbon Cathodes for Lithium-Ion Batteries. *ACS Nano* **2013**, *7* (12), 10995-11003. DOI: 10.1021/nn404601h From NLM PubMed-not-MEDLINE.

(18) Li, S.; Jiang, J.; Dong, Z.; Wu, J.; Cheng, Z.; Zhu, H.; Fan, Z.; Wang, Y.; Leng, D. Ferroconcrete-Inspired Construction of Self-Supporting $Li_2S$ Cathode for High-Performance Lithium–Sulfur Batteries. *Microporous Mesoporous Mater.* **2020**, *293*. DOI: 10.1016/j.micromeso.2019.109822.

(19) Jiang, M.; Liu, G.; Zhang, Q.; Zhou, D.; Yao, X. Ultrasmall $Li_2S$-Carbon Nanotube Nanocomposites for High-Rate All-Solid-State Lithium-Sulfur Batteries. *ACS Appl. Mater.*

*Interfaces* **2021**, *13* (16), 18666-18672. DOI: 10.1021/acsami.1c00511 From NLM PubMed-not-MEDLINE.

(20) Yuan, H.; Chen, X.; Zhou, G.; Zhang, W.; Luo, J.; Huang, H.; Gan, Y.; Liang, C.; Xia, Y.; Zhang, J.; Wang, J.; Tao, X. Efficient Activation of $Li_2S$ by Transition Metal Phosphides Nanoparticles for Highly Stable Lithium–Sulfur Batteries. *ACS Energy Lett.* **2017**, *2* (7), 1711-1719. DOI: 10.1021/acsenergylett.7b00465.

(21) Yang, Q.; Wei, X.; Cao, X.; Chen, L.; Song, L.; Kong, L.; Sun, W.; Xie, K.; Song, Y. Unveiling the Synergistic Catalysis Essence of Trimetallic Fe-Co-Ni Phosphides for Lithium–Sulfur Chemistry. *SSRN Electronic Journal* **2022**. DOI: 10.2139/ssrn.4169696.

(22) Du, R.; Xiao, K.; Li, B.; Han, X.; Zhang, C.; Wang, X.; Zuo, Y.; Guardia, P.; Li, J.; Chen, J.; Arbiol, J.; Cabot, A. Controlled Oxygen Doping in Highly Dispersed Ni-Loaded g-$C_3N_4$ Nanotubes for Efficient Photocatalytic $H_2O_2$ Production. *Chem. Eng. J.* **2022**, *441*. DOI: 10.1016/j.cej.2022.135999.

(23) Zhang, C.; Du, R.; Martí-Sánchez, S.; Xiao, K.; Yang, D.; Zhang, C.; Li, C.; Zeng, G.; Chang, X.; He, R.; Arbiol, J.; Li, J.; Jacas Biendicho, J.; Cabot, A. Tubular $C_3N_4$ Nanotubes as Metal-Free Sulfur Hosts toward Stable Lithium–Sulfur Batteries. *Energies* **2023**, *16* (12). DOI: 10.3390/en16124545.

(24) Zhang, C.; Du, R.; Biendicho, J. J.; Yi, M.; Xiao, K.; Yang, D.; Zhang, T.; Wang, X.; Arbiol, J.; Llorca, J.; Zhou, Y.; Morante, J. R.; Cabot, A. Tubular CoFeP@CN as a Mott–Schottky Catalyst with Multiple Adsorption Sites for Robust Lithium−Sulfur Batteries. *Adv. Energy Mater.* **2021**, *11* (24). DOI: 10.1002/aenm.202100432.

(25) Wang, J.; Meng, Z.; Yang, W.; Yan, X.; Guo, R.; Han, W. Q. Facile Synthesis of rGO/g-$C_3N_4$/CNT Microspheres Via an Ethanol-Assisted Spray-Drying Method for High-Performance

Lithium-Sulfur Batteries. *ACS Appl. Mater. Interfaces* **2019**, *11* (1), 819-827. DOI: 10.1021/acsami.8b17590 From NLM PubMed-not-MEDLINE.

(26) Zeng, D.; Xu, W.; Ong, W.-J.; Xu, J.; Ren, H.; Chen, Y.; Zheng, H.; Peng, D.-L. Toward Noble-Metal-Free Visible-Light-Driven Photocatalytic Hydrogen Evolution: Monodisperse Sub–15 nm $Ni_2P$ Nanoparticles Anchored on Porous g-$C_3N_4$ Nanosheets to Engineer 0D-2D Heterojunction Interfaces. *Appl. Catal., B* **2018**, *221*, 47-55. DOI: 10.1016/j.apcatb.2017.08.041.

(27) Zhang, F.; Zhang, J.; Li, J.; Jin, X.; Li, Y.; Wu, M.; Kang, X.; Hu, T.; Wang, X.; Ren, W.; Zhang, G. Modulating Charge Transfer Dynamics for g-$C_3N_4$ through a Dimension and Interface Engineered Transition Metal Phosphide Co-Catalyst for Efficient Visible-Light Photocatalytic Hydrogen Generation. *J. Mater. Chem. A* **2019**, *7* (12), 6939-6945. DOI: 10.1039/c9ta00765b.

(28) Cao, S.; Wang, C. J.; Fu, W. F.; Chen, Y. Metal Phosphides as Co-Catalysts for Photocatalytic and Photoelectrocatalytic Water Splitting. *ChemSusChem* **2017**, *10* (22), 4306-4323. DOI: 10.1002/cssc.201701450 From NLM PubMed-not-MEDLINE.

(29) Liu, J.; Meyns, M.; Zhang, T.; Arbiol, J.; Cabot, A.; Shavel, A. Triphenyl Phosphite as the Phosphorus Source for the Scalable and Cost-Effective Production of Transition Metal Phosphides. *Chem. Mater.* **2018**, *30* (5), 1799-1807. DOI: 10.1021/acs.chemmater.8b00290.

(30) Ye, F.; Liu, M.; Yan, X.; Li, J.; Pan, Z.; Li, H.; Zhang, Y. In Situ Electrochemically Derived Amorphous-$Li_2S$ for High Performance $Li_2S$/Graphite Full Cell. *Small* **2018**, *14* (17), e1703871. DOI: 10.1002/smll.201703871 From NLM PubMed-not-MEDLINE.

(31) Borchert, H.; Shevchenko, E. V.; Robert, A.; Mekis, I.; Kornowski, A.; Grubel, G.; Weller, H. Determination of Nanocrystal Sizes: A Comparison of TEM, SAXS, and XRD Studies of Highly Monodisperse $CoPt_3$ Particles. *Langmuir* **2005**, *21* (5), 1931-1936. DOI: 10.1021/la0477183 From NLM PubMed-not-MEDLINE.

(32) Dai, H.; Gao, X.; Liu, E.; Yang, Y.; Hou, W.; Kang, L.; Fan, J.; Hu, X. Synthesis and Characterization of Graphitic Carbon Nitride Sub-Microspheres Using Microwave Method under Mild Condition. *Diamond Relat. Mater.* **2013**, *38*, 109-117. DOI: 10.1016/j.diamond.2013.06.012.

(33) Wang, M. Q.; Ye, C.; Liu, H.; Xu, M.; Bao, S. J. Nanosized Metal Phosphides Embedded in Nitrogen-Doped Porous Carbon Nanofibers for Enhanced Hydrogen Evolution at All pH Values. *Angew. Chem. Int. Ed. Engl.* **2018**, *57* (7), 1963-1967. DOI: 10.1002/anie.201710150 From NLM PubMed-not-MEDLINE.

(34) Sing, K. S. W. Reporting Physisorption Data for Gas/Solid Systems with Special Reference to the Determination of Surface Area and Porosity (Recommendations 1984). *Pure Appl. Chem.* **1985**, *57* (4), 603-619. DOI: 10.1351/pac198557040603.

(35) Liu, D.; Kong, Z.; Liu, X.; Fu, A.; Wang, Y.; Guo, Y. G.; Guo, P.; Li, H.; Zhao, X. S. Spray-Drying-Induced Assembly of Skeleton-Structured $SnO_2$/Graphene Composite Spheres as Superior Anode Materials for High-Performance Lithium-Ion Batteries. *ACS Appl. Mater. Interfaces* **2018**, *10* (3), 2515-2525. DOI: 10.1021/acsami.7b15916 From NLM PubMed-not-MEDLINE.

(36) Ma, Z.; Gao, J.; Weng, X.; Yang, S.; Peng, K. Synthesis and Mechanism of Aluminum Silicate Mesoporous Materials by F108 Template. *Mater. Sci.-Pol.* **2020**, *38* (4), 566-576. DOI: 10.2478/msp-2020-0067.

(37) Horikawa, T.; Do, D. D.; Nicholson, D. Capillary Condensation of Adsorbates in Porous Materials. *Adv. Colloid Interface Sci.* **2011**, *169* (1), 40-58. DOI: 10.1016/j.cis.2011.08.003.

(38) Liu, B.; Liu, M.; Tian, L.; Guo, F.; Xia, Y.; Wang, T.; Hu, W.; Guan, R. A Novel Route to Porous N-Doping Carbon Grafted Carbon Nitride for Enhanced Photocatalytic Activity on $CO_2$ Reduction. *Appl. Surf. Sci.* **2021**, *540*. DOI: 10.1016/j.apsusc.2020.148411.

(39) Wang, X. J.; Tian, X.; Sun, Y. J.; Zhu, J. Y.; Li, F. T.; Mu, H. Y.; Zhao, J. Enhanced Schottky Effect of a 2D-2D CoP/g-$C_3N_4$ Interface for Boosting Photocatalytic $H_2$ Evolution. *Nanoscale* **2018**, *10* (26), 12315-12321. DOI: 10.1039/c8nr03846e From NLM PubMed-not-MEDLINE.

(40) Zhao, H.; Wang, J.; Dong, Y.; Jiang, P. Noble-Metal-Free Iron Phosphide Cocatalyst Loaded Graphitic Carbon Nitride as an Efficient and Robust Photocatalyst for Hydrogen Evolution under Visible Light Irradiation. *ACS Sustainable Chem. Eng.* **2017**, *5* (9), 8053-8060. DOI: 10.1021/acssuschemeng.7b01665.

(41) Xue, L.; Zeng, L.; Kang, W.; Chen, H.; Hu, Y.; Li, Y.; Chen, W.; Lei, T.; Yan, Y.; Yang, C.; Hu, A.; Wang, X.; Xiong, J.; Zhang, C. 3D Printed Li–S Batteries with In Situ Decorated $Li_2S$/C Cathode: Interface Engineering Induced Loading-Insensitivity for Scaled Areal Performance. *Adv. Energy Mater.* **2021**, *11* (14). DOI: 10.1002/aenm.202100420.

(42) Wu, J.; Li, C.; Zhang, W.; Han, J.; Wang, L.; Wang, S.; Wang, Y. Bimetallic Manganese Cobalt Phosphide Nanodots–Modified Graphitic Carbon Nitride for High-Performance Hydrogen Production. *Energy Technol.* **2019**, *7* (5). DOI: 10.1002/ente.201800927.

(43) Wang, J.; Zhang, J.; Duan, S.; Li, T.; Jia, L.; Liu, H.; Li, L.; Cheng, S.; Hu, H.; Huang, M.; Hu, H.; Zhang, S.; Xiao, Q.; Lin, H. Interfacial Lithium-Nitrogen Bond Catalyzes Sulfide Oxidation Reactions in High-Loading $Li_2S$ Cathode. *Chem. Eng. J.* **2022**, *429*. DOI: 10.1016/j.cej.2021.132352.

(44) Chen, Y.; Zhang, W.; Zhou, D.; Tian, H.; Su, D.; Wang, C.; Stockdale, D.; Kang, F.; Li, B.; Wang, G. Co-Fe Mixed Metal Phosphide Nanocubes with Highly Interconnected-Pore Architecture as an Efficient Polysulfide Mediator for Lithium-Sulfur Batteries. *ACS Nano* **2019**, *13* (4), 4731-4741. DOI: 10.1021/acsnano.9b01079 From NLM PubMed-not-MEDLINE.

(45) Zhu, Q.; Qiu, B.; Duan, H.; Gong, Y.; Qin, Z.; Shen, B.; Xing, M.; Zhang, J. Electron Directed Migration Cooperated with Thermodynamic Regulation over Bimetallic NiFeP/g-$C_3N_4$ for Enhanced Photocatalytic Hydrogen Evolution. *Appl. Catal., B* **2019**, *259*. DOI: 10.1016/j.apcatb.2019.118078.

(46) Zhong, Y.; Yin, L.; He, P.; Liu, W.; Wu, Z.; Wang, H. Surface Chemistry in Cobalt Phosphide-Stabilized Lithium-Sulfur Batteries. *J. Am. Chem. Soc.* **2018**, *140* (4), 1455-1459. DOI: 10.1021/jacs.7b11434 From NLM PubMed-not-MEDLINE.

(47) Li, J.; Li, L.; Ma, X.; Han, X.; Xing, C.; Qi, X.; He, R.; Arbiol, J.; Pan, H.; Zhao, J.; Deng, J.; Zhang, Y.; Yang, Y.; Cabot, A. Selective Ethylene Glycol Oxidation to Formate on Nickel Selenide with Simultaneous Evolution of Hydrogen. *Adv. Sci.* **2023**, *10* (15), e2300841. DOI: 10.1002/advs.202300841 From NLM PubMed-not-MEDLINE.

(48) Liu, H.; Zeng, P.; Yu, H.; Zhou, X.; Li, Z.; Chen, M.; Miao, C.; Chen, G.; Wu, T.; Wang, X. Enhancing the Electrochemical Performances of $Li_2S$-Based Cathode through Conductive Interface Design and Addition of Mixed Conductive Materials. *Electrochim. Acta* **2021**, *396*. DOI: 10.1016/j.electacta.2021.139238.

(49) Son, Y.; Lee, J.-S.; Son, Y.; Jang, J.-H.; Cho, J. Recent Advances in Lithium Sulfide Cathode Materials and Their Use in Lithium Sulfur Batteries. *Adv. Energy Mater.* **2015**, *5* (16). DOI: 10.1002/aenm.201500110.

(50) Wang, D.-h.; Xie, D.; Xia, X.-h.; Zhang, X.-q.; Tang, W.-j.; Zhong, Y.; Wu, J.-b.; Wang, X.-l.; Tu, J.-p. A 3D Conductive Network with High Loading $Li_2S$@C for High Performance Lithium–Sulfur Batteries. *J. Mater. Chem. A* **2017**, *5* (36), 19358-19363. DOI: 10.1039/c7ta06090d.

(51) Li, Z.; Zhang, S.; Zhang, C.; Ueno, K.; Yasuda, T.; Tatara, R.; Dokko, K.; Watanabe, M. One-Pot Pyrolysis of Lithium Sulfate and Graphene Nanoplatelet Aggregates: In Situ Formed

$Li_2S$/Graphene Composite for Lithium-Sulfur Batteries. *Nanoscale* **2015**, *7* (34), 14385-14392. DOI: 10.1039/c5nr03201f From NLM PubMed-not-MEDLINE.

(52) Chen, X.; Ding, X.; Wang, C.; Feng, Z.; Xu, L.; Gao, X.; Zhai, Y.; Wang, D. A Multi-Shelled CoP Nanosphere Modified Separator for Highly Efficient Li-S Batteries. *Nanoscale* **2018**, *10* (28), 13694-13701. DOI: 10.1039/c8nr03854f From NLM PubMed-not-MEDLINE.

(53) Liang, X.; Yun, J.; Xu, K.; Xiang, H.; Wang, Y.; Sun, Y.; Yu, Y. A Multi-Layered $Ti_3C_2/Li_2S$ Composite as Cathode Material for Advanced Lithium-Sulfur Batteries. *J. Energy Chem.* **2019**, *39*, 176-181. DOI: 10.1016/j.jechem.2019.02.002.

(54) Zhang, J.; Wang, J.; Qian, M.; Zhao, B.; Wang, R.; Hao, X.; Huang, X.; Shao, R.; Xing, Z.; Xie, J.; Xu, B.; Su, Y.; Wu, F.; Tan, G. Lithiothermic-Synchronous Construction of Mo-$Li_2S$-Graphene Nanocomposites for High-Energy $Li_2S$//Si─C Battery. *Adv. Funct. Mater.* **2021**, *32* (1). DOI: 10.1002/adfm.202108305.

(55) Chen, M.; Zhao, X.; Li, Y.; Zeng, P.; Liu, H.; Yu, H.; Wu, M.; Li, Z.; Shao, D.; Miao, C.; Chen, G.; Shu, H.; Pei, Y.; Wang, X. Kinetically Elevated Redox Conversion of Polysulfides of Lithium-Sulfur Battery Using a Separator Modified with Transition Metals Coordinated g-$C_3N_4$ with Carbon-Conjugated. *Chem. Eng. J.* **2020**, *385*. DOI: 10.1016/j.cej.2019.123905.

(56) Yang, Y.; Zheng, G.; Misra, S.; Nelson, J.; Toney, M. F.; Cui, Y. High-Capacity Micrometer-Sized $Li_2S$ Particles as Cathode Materials for Advanced Rechargeable Lithium-Ion Batteries. *J. Am. Chem. Soc.* **2012**, *134* (37), 15387-15394. DOI: 10.1021/ja3052206 From NLM PubMed-not-MEDLINE.

(57) Wu, X.; Liu, N.; Wang, M.; Qiu, Y.; Guan, B.; Tian, D.; Guo, Z.; Fan, L.; Zhang, N. A Class of Catalysts of BiOX (X = Cl, Br, I) for Anchoring Polysulfides and Accelerating Redox Reaction

in Lithium Sulfur Batteries. *ACS Nano* **2019**, *13* (11), 13109-13115. DOI: 10.1021/acsnano.9b05908 From NLM PubMed-not-MEDLINE.

(58) Zhang, L.; Huang, H.; Xia, Y.; Liang, C.; Zhang, W.; Luo, J.; Gan, Y.; Zhang, J.; Tao, X.; Fan, H. J. High-Content of Sulfur Uniformly Embedded in Mesoporous Carbon: A New Electrodeposition Synthesis and an Outstanding Lithium–Sulfur Battery Cathode. *J. Mater. Chem. A* **2017**, *5* (12), 5905-5911. DOI: 10.1039/c7ta00328e.

(59) Ye, F.; Noh, H.; Lee, H.; Kim, H.-T. An Ultrahigh Capacity Graphite/$Li_2S$ Battery with Holey-$Li_2S$ Nanoarchitectures. *Adv. Sci.* **2018**, *5* (7). DOI: 10.1002/advs.201800139.

(60) Zhang, J.; Shi, Y.; Ding, Y.; Peng, L.; Zhang, W.; Yu, G. A Conductive Molecular Framework Derived $Li_2S$/N,P-Codoped Carbon Cathode for Advanced Lithium–Sulfur Batteries. *Adv. Energy Mater.* **2017**, *7* (14). DOI: 10.1002/aenm.201602876.

(61) Chen, L.; Liu, Y.; Zhang, F.; Liu, C.; Shaw, L. L. PVP-Assisted Synthesis of Uniform Carbon Coated $Li_2S$/CB for High-Performance Lithium-Sulfur Batteries. *ACS Appl. Mater. Interfaces* **2015**, *7* (46), 25748-25756. DOI: 10.1021/acsami.5b07331 From NLM PubMed-not-MEDLINE.

(62) Zhou, G.; Wang, D. W.; Yin, L. C.; Li, N.; Li, F.; Cheng, H. M. Oxygen Bridges between NiO Nanosheets and Graphene for Improvement of Lithium Storage. *ACS Nano* **2012**, *6* (4), 3214-3223. DOI: 10.1021/nn300098m From NLM Medline.

(63) Fan, B.; Guan, Z.; Wang, H.; Wu, L.; Li, W.; Zhang, S.; Xue, B. Electrochemical Processes in All-Solid-State Li-S Batteries Studied by Electrochemical Impedance Spectroscopy. *Solid State Ionics* **2021**, *368*. DOI: 10.1016/j.ssi.2021.115680.

(64) Fan, Q.; Jiang, J.; Zhang, S.; Zhou, T.; Pang, W. K.; Gu, Q.; Liu, H.; Guo, Z.; Wang, J. Accelerated Polysulfide Redox in Binder-Free $Li_2S$ Cathodes Promises High-Energy-Density Lithium–Sulfur Batteries. *Adv. Energy Mater.* **2021**, *11* (32). DOI: 10.1002/aenm.202100957.

(65) Gu, L.-L.; Gao, J.; Wang, C.; Qiu, S.-Y.; Wang, K.-X.; Gao, X.-T.; Sun, K.-N.; Zuo, P.-J.; Zhu, X.-D. Thin Carbon Layer Enveloped Cobalt–Iron Oxide Nanocages as a High-Efficiency Sulfur Container for Li–S Batteries. *J. Mater. Chem. A* **2020**, *8* (39), 20604-20611. DOI: 10.1039/d0ta07579e.

(66) Ganesan, A.; Varzi, A.; Passerini, S.; Shaijumon, M. M. Graphene Derived Carbon Confined Sulfur Cathodes for Lithium-Sulfur Batteries: Electrochemical Impedance Studies. *Electrochim. Acta* **2016**, *214*, 129-138. DOI: 10.1016/j.electacta.2016.08.030.

(67) Song, J.; Noh, H.; Lee, J.; Nah, I.-W.; Cho, W.-I.; Kim, H.-T. In Situ Coating of Poly(3,4-ethylenedioxythiophene) on Sulfur Cathode for High Performance Lithium–Sulfur Batteries. *J. Power Sources* **2016**, *332*, 72-78. DOI: 10.1016/j.jpowsour.2016.09.092.

(68) Karuppiah, S.; Keller, C.; Kumar, P.; Jouneau, P. H.; Aldakov, D.; Ducros, J. B.; Lapertot, G.; Chenevier, P.; Haon, C. A Scalable Silicon Nanowires-Grown-On-Graphite Composite for High-Energy Lithium Batteries. *ACS Nano* **2020**, *14* (9), 12006-12015. DOI: 10.1021/acsnano.0c05198 From NLM PubMed-not-MEDLINE.

(69) Keller, C.; Karuppiah, S.; Raaen, M.; Wang, J.; Perrenot, P.; Aldakov, D.; Reiss, P.; Haon, C.; Chenevier, P. Low-Cost Tin Compounds as Seeds for the Growth of Silicon Nanowire–Graphite Composites Used in High-Performance Lithium-Ion Battery Anodes. *ACS Appl. Energy Mater.* **2023**, *6* (10), 5249-5258. DOI: 10.1021/acsaem.3c00178.

(70) Guo, J.; Omar, A.; Urbanski, A.; Oswald, S.; Uhlmann, P.; Giebeler, L. Electrochemical Behavior of Microparticulate Silicon Anodes in Ether-Based Electrolytes: Why Does $LiNO_3$ Affect Negatively? *ACS Appl. Energy Mater.* **2019**, *2* (6), 4411-4420. DOI: 10.1021/acsaem.9b00590.

*Supporting Information*

# Nanostructured $Li_2S$ Cathodes for Silicon-Sulfur Batteries

*Hamid Mollania,* [a,b] *Chaoqi Zhang,* [b] *Ruifeng Du,* [b] *Xueqiang Qi,*,*[c] *Junshan Li,* [d] *Sharona Horta,* [e] *Maria Ibañez,* [e] *Caroline Keller,* [f] *Pascale Chenevier,* [f] *Majid Oloomi-Buygi,*,*[a] *and Andreu Cabot *,*[b,g]

[a] Ferdowsi University of Mashhad, Department of Electrical Engineering, Mashhad 9177948974, Iran.

[b] Catalonia Institute for Energy Research - IREC, Sant Adrià del Besòs, Barcelona 08930, Spain.

[c] College of Chemistry and Chemical Engineering, Chongqing University of Technology, Chongqing 400054, China.

[d] Institute for Advanced Study, Chengdu University, 610106, Chengdu, China.

[e] Institute of Science and Technology Austria (ISTA), Am Campus 1, Klosterneuburg 3400, Austria.

[f] Université Grenoble Alpes, CEA, CNRS, IRIG, SYMMES, STEP, 38000 Grenoble, France.

[g] ICREA, Pg. Lluís Companys 23, 08010 Barcelona, Catalonia, Spain.

* Corresponding authors: acabot@irec.cat (A. Cabot), m.oloomi@um.ac.ir (M. Oloomi-Buygi), xqqi@cqut.edu.cn (X. Qi)

# 1. Experimental Methods

## 1.1. Synthesis of KB-Co

In a typical synthesis, 2 g of Ketjen black (KB, EC600JD) and 1 g of $Co(NO_3)_2 \cdot 6H_2O$ were dispersed in the solution of 130 ml deionized water and 20 ml anhydrous ethanol. For 10 hours, the mixture was stirred continuously at room temperature. Afterward, the mixture was dried slowly under the vacuum in the fume hood and stored in a 65 °C oven for a night. Finally, the dried sample was then placed in a tubular oven and calcined under the Ar flow at 900 °C for 3 h with a heating rate of 10 °C/min.

## 1.2. Growth of Graphite-Silicon-Nanowire composite (Gt-SiNW)

SiNWs were grown in a stainless-steel pressure reactor (150 $cm^3$) as described in our previous work.[1-3] A suspension of $SnO_2$ NPs (≤50 nm, 80 mg, from Sigma Aldrich) in water/ethanol (5 mL) was added to 800 mg of graphite (TIMCAL) in a mortar heated at 80 °C. The mixture was ground with a pestle until complete drying. The $SnO_2$-loaded graphite was sealed with 12mL diphenylsilane in the reactor under vacuum and heated at 390 °C for 5 h. After cooling down, the black powder was washed thoroughly with dichloromethane and dried at 80 °C, yielding 1.1g of product.

## 1.3. Materials Characterization

XRD measurements were carried out on a D8 Advance diffractometer (Bruker AXS) with Cu Kα radiation (λ = 1.5406 Å) from 20 to 80° operating at 40 kV and 40 mA. As the $Li_2S$ is moisture sensitive, for samples containing $Li_2S$, the sample holders were filled inside the glovebox and a Kapton tape was used to protect the samples against air moisture during measurements. The morphology of samples was examined by the Field Emission Scanning Electron Microscope (FE-SEM, Carl Zeiss Auriga 60) coupled with Oxford INCA Instruments Energy Dispersive Spectrometer (EDS) operated at 20 kV. HRTEM, STEM, and EDS studies were conducted using a JEM-2800 (JEOL Ltd.) field emission gun microscope operated at 200 kV. High-resolution TEM (HRTEM) images were acquired at room temperature and captured directly through the CCD detector without additional processing or filtering. Energy-dispersive X-ray spectroscopy (EDX) mapping was performed in conjunction with the HAADF-STEM imaging to determine the elemental composition and distribution of the samples. The bonded structures of the samples were

characterized by X-ray photoelectron spectroscopy (XPS) using an ESCALAB 250Xi electron spectrometer with a monochromatic AlKa X-ray radiation source under a base pressure of $2 \times 10^{-7}$ Pa. The Fermi level position was corrected by setting the main C 1S peak at 284.8 eV. The content of $Li_2S$ in the samples was carried out on a SETARAM Sensys Evo Thermogravimetric Analyzer (TG-DSC), which is equipped with the atmospheric control. The specific surface area of the samples was determined with $N_2$ adsorption/desorption isotherms on TriStar II 3020 Micromeritics surface area analyzer. The sample loading procedure for the $N_2$ adsorption-desorption test is carried out in the Ar-filled glove box due to the high reactivity of $Li_2S$ with moisture. The optical properties of samples were determined with Lambda 950 UV-Vis-NIR Spectrophotometer (Perkin Elmer).

### 1.4. Cell assembly and electrochemical measurements

To test the cathode performances, CR2032 coin-type cells were assembled, in which lithium foils were used as anode, Celgard 2400 membranes as separators, and $Li_2S$-host electrode as the cathode. The electrolyte contains 1.0 M lithium bis(trifluoromethanesulfonyl)imide (LiTFSI), 1,2-dimethoxy ethane (DME), 1,3-dioxolane (DOL) (v/v = 1/1), and 0.2 M of $LiNO_3$. As $Li_2S$ is moisture sensitive all the coin cell assembly process was done inside the glove box with 0.1 ppm $O_2$ and 0.0 ppm $H_2O$ level. To prepare the cathodes, doctor blade methods were used. Typically, $Li_2S$-host composites, dried super-P conductive carbon black, and PVDF binder (weight ratio = 8:1:1) were well mixed into anhydrous 1-methyl-2-pyrrolidone (anhydrous NMP, 99.5%, Sigma Aldrich). Then the slurry was cast on the aluminum foil and dried at 65 °C overnight inside the glove box. After that, the foil was punched into disks with a diameter of 12.0 mm. $Li_2S$ loading was about 1.2-1.4 $mg_{Li_2S}cm^{-2}$ and for each coin cell 18-20 µL of electrolyte was used. The cells were galvanostatically cycled at room temperature at a voltage window of 1.7-3.6 V for the first activation cycle and 1.7-2.8 V for the other cycles on a Neware BTS4008 battery tester. Cyclic voltammetry (CV) and electrochemical impedance spectroscopy (EIS) tests were performed on BCS-810 (Bio-Logic) battery tester. The EIS analysis was performed with a sinusoidal voltage in the frequency range from 100 kHz to 0.1 Hz and an amplitude of 10 mV.

To prepare the anodes, doctor blade methods were used. Typically, Gt-SiNW composites, super-P conductive carbon black, and Sodium carboxymethyl cellulose (CMC, Sigma Aldrich) binder (weight ratio = 8:1:1) were well mixed into pure distilled water. Then the slurry was cast on the copper foil and dried at 80 °C overnight inside the vacuum oven. After that, the foil was punched

into disks with a diameter of 12.0 mm. Gt-SiNW loading was about 2.3 to 3.3 mg $cm^{-2}$ for different coin cells. The carbonate electrolyte was 1.2 M $LiPF_6$ in ethylene carbonate/dimethyl carbonate/ethyl methyl carbonate (EC/DMC/EMC (2/3/5 vol%)) containing 2wt.% vinylene carbonate (VC), 2wt.% fluoroethylene carbonate (FEC). The ether-based electrolyte and the separators were the same as the cathode. The CR2032 cells were galvanostatically cycled at room temperature at a voltage window of 0.01-1 V on an Arbin MSTAT (multi-channel potentiostat/galvanostat) instrument.

For full cell preparation, first, the Gt-SiNW anodes were lithiated from the OCV to 0.01 V by CCCV protocol for one cycle. Then the cell was disassembled inside the Ar-filled glove box and the prelithiated Gt-SiNW electrode was used as the anode. The anode was coupled with $Li_2S$-CoFeP-CN cathode in CR2032 coin cells with the same separator and the electrolyte used for the cathode half cell test. In detail, by considering the theoretical capacity of $Li_2S$ cathode and assuming that 60% of the initial capacity of Gt-SiNW anode is used for prelithiation, the anode/cathode loading was balanced to be sure that the remaining anode capacity after lithiation matched 1.2:1 (Gt-SiNW/$Li_2S$-CoFeP-CN).

### 1.5. Adsorption test of LiPSs

The $Li_2S_6$ solution was prepared by adding $Li_2S$ and sulfur powder with the molar ratio of 1:5 into a DME/DOL (v/v, 1:1), and stirring at 45 °C for 12 h inside the glovebox.

### 1.6. Theoretical Computations

Spin-polarized density functional theory (DFT) calculations were performed with the Perdew-Burke-Ernzerhof (PBE) generalized gradient approximation (GGA) exchange-correlation functional.[4] The core electrons were treated with Ultrasoft Pseudopotentials.[5] Three layers of CoFeP (112) containing 144 atoms (including 48 Co, 48 Fe, and 48 P atoms) and three layers of CoFeP (020) that contains the same atoms were chosen as our models, and a supercell of g-$C_3N_4$ containing 56 atoms was chosen to be studied comparatively. A vacuum layer of 20 Å thickness was used in the z-direction to create the surface. All the atoms were allowed to be relaxed in the calculations. A cutoff energy of 400 eV was used for the plane-wave basis set. The threshold of self-consistent-field energy convergence was $1x10^{-5}$ eV/atom. The convergence criterion for the structural optimizations was a maximum force of 0.03 eV/Å and a maximum displacement of 0.001 Å. 2×2×1 k-points using the Monkhorst-Pack scheme grid were used to sample the Brillouin zone.[6]

The transferred energies of the Li atom both on the CoFeP surfaces and the g-$C_3N_4$ surface were calculated through the analysis of adsorption energy at the fixed points along the artificial routes. The adsorption energy of the Li atom ($E_{ads}$) was calculated according to equation (S1):

$$E_{ads} = E_{Li\text{-}Ca} - (E_{Li} + E_{Ca}) \quad \text{(S1)}$$

Where $E_{Li\text{-}Ca}$ represents the total energy of the system with Li species (including $Li_2S$, LiS, and Li) adsorbing on the CoFeP surfaces or g-$C_3N_4$ surface. $E_{Ca}$ is the total energy of the clean CoFeP surfaces or g-$C_3N_4$ surface, and $E_{Li}$ is the energy of pure Li species (including $Li_2S$, LiS, and Li).

## 1.7. Determination of CoFeP weight percentage in CoFeP-CN composite

As TGA was performed in dry air, the weight change of the CoFeP-CN composite is due to the oxidation of CoFeP-CN to $Co_2O_3$, $Fe_2O_3$, and $P_2O_5$ and the decomposition of g-$C_3N_4$ to $CO_2$ and $N_2$. Therefore, the weight percentage of CoFeP and g-$C_3N_4$ can be calculated by the following equations:

$$M_{Co_{1.4}Fe_1P_2} \times n_{Co_{1.4}Fe_1P_2} + M_{C_3N_4} \times n_{C_3N_4} = m_{\,initial\,(CoFeP-CN)} \quad \text{(S2)}$$

$$M_{Co_2O_3} \times n_{Co_2O_3} + M_{Fe_2O_3} \times n_{Fe_2O_3} + M_{P_2O_5} \times n_{P_2O_5} = m_{\,Final} \quad \text{(S3)}$$

Where the molecular weights $M_{Co_{1.4}Fe_1P_2}$, $M_{C_3N_4}$, $M_{Co_2O_3}$, $M_{Fe_2O_3}$, and $M_{P_2O_5}$ is 200.299, 92.0589, 165.8646, 159.6882, and 141.9445, respectively. By applying $n_{Co_2O_3} = 0.5 \times 1.4 n_{Co_{1.4}Fe_1P_2}$, $n_{Fe_2O_3} = 0.5 n_{Co_{1.4}Fe_1P_2}$, and $n_{P_2O_5} = 0.5 \times 2 n_{Co_{1.4}Fe_1P_2}$, the number of moles of CoFeP NCs ($n_{Co_{1.4}Fe_1P_2}$) can be obtained from equation S3 and the weight percentage of $Co_{1.4}Fe_1P_2$ can be calculated. It should be mentioned, based on the EDX analysis of CoFeP-CN samples, the atomic ratio of Co:Fe:P is considered to be 1.4:1:2.

## 1.8. Determination of $Li_2S$ weight percentage from TGA analysis

Based on the S2 and S3 equations and considering the weight fraction of g-$C_3N_4$ to CoFeP ($\frac{wt.\%_{C3N4}}{wt.\%_{CoFeP}}$), the equations S2 and S3 can be written also for the TGA analysis of $Li_2S$-CoFeP-CN composite as follows:

$$M_{\mathrm{Li_2S}} \times n_{\mathrm{Li_2S}} + (1 + \frac{\text{wt.}\%_{\mathrm{C3N4}}}{\text{wt.}\%_{\mathrm{CoFeP}}}) \times M_{\mathrm{Co_{1.4}Fe_1P_2}} \times n_{\mathrm{Co_{1.4}Fe_1P_2}} = m_{\,initial(Li_2S-CoFeP-CN)} \quad \text{(S4)}$$

$$M_{\mathrm{Li_2SO_4}} \times n_{\mathrm{Li_2SO_4}} + M_{\mathrm{Co_2O_3}} \times n_{\mathrm{Co_2O_3}} + M_{\mathrm{Fe_2O_3}} \times n_{\mathrm{Fe_2O_3}} + M_{\mathrm{P_2O_5}} \times n_{\mathrm{P_2O_5}} = m_{\,Final} \quad \text{(S5)}$$

Given $n_{\mathrm{Li_2SO_4}} = n_{\mathrm{Li_2S}}$, $M_{\mathrm{Li_2S}} = 45.947$, and $M_{\mathrm{Li_2SO_4}} = 109.9446$, the weight percentage of $Li_2S$ can be calculated.

To further validate the above equations, the weight percentage of $Li_2S$ was also calculated just based on the initial and final weights in TGA analysis (formula S6). In the S6 formula, we just assumed that all the initial $Li_2S$ has oxidized to $Li_2SO_4$ at the end of TGA analysis.

$$\begin{cases} \mathrm{W_{B,F}} - \mathrm{W_{Li_2SO_4}} = \mathrm{W_{B,F}} - \mathrm{M} \times \mathrm{W_{Li_2S}} = \mathrm{W_{A,F}} \\ \mathrm{W_{A,F}} = \left(\frac{\mathrm{W_{A,F}}}{\mathrm{W_{A,I}}}\right) \times \mathrm{W_{A,I}} = \left(\frac{\mathrm{W_{A,F}}}{\mathrm{W_{A,I}}}\right) \times \left(\mathrm{W_{B,I}} - \mathrm{W_{Li_2S}}\right) \cdots \end{cases}$$

$$\ldots \rightarrow wt.\%\,(Li_2S) = \frac{\mathrm{W_{Li_2S}}}{\mathrm{W_{B,I}}} \times 100 = \frac{\left(\frac{\mathrm{W_{B,F}}}{\mathrm{W_{B,I}}}\right) - \left(\frac{\mathrm{W_{A,F}}}{\mathrm{W_{A,I}}}\right)}{M - \left(\frac{\mathrm{W_{A,F}}}{\mathrm{W_{A,I}}}\right)} \times 100 \quad \text{(S6)}$$

Where A refers to CoFeP-CN, B refers to $Li_2S$-CoFeP-CN, $\mathrm{W_{A,I}}$ refers to the Initial weight of composite A, $\mathrm{W_{A,F}}$ refers to the final weight of composite A, $\mathrm{M} = {}^{\mathrm{M_{Li_2SO_4}}}/_{\mathrm{M_{Li_2S}}}$, and $\mathrm{W_{Li_2SO_4}} = \mathrm{M} \times \mathrm{W_{Li_2S}}$.

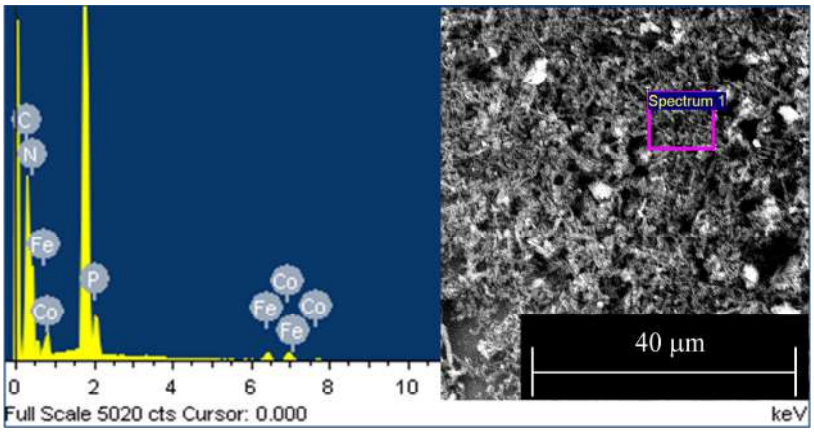


**Figure S1.** SEM-EDX spectrum of CoFeP-CN composite.

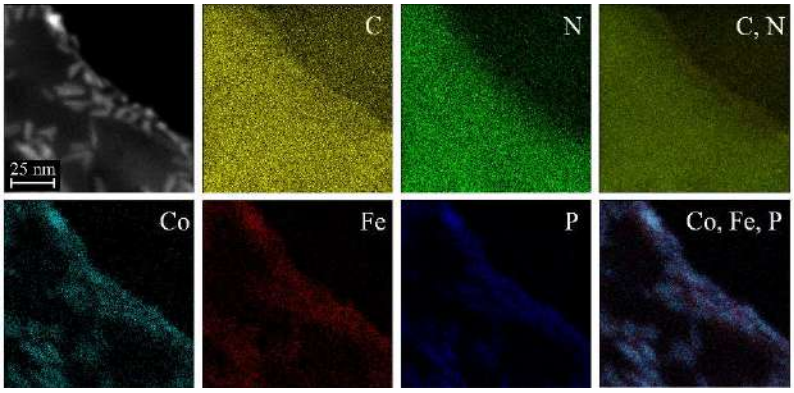


**Figure S2.** Annular dark-field-scanning (ADF)-STEM image and corresponding EDX images obtained from the thin areas of CoFeP-CN. The images show that CoFeP nanoparticles have bright contrast and EDX images verify the presence of CoFeP nanoparticles on g-$C_3N_4$.

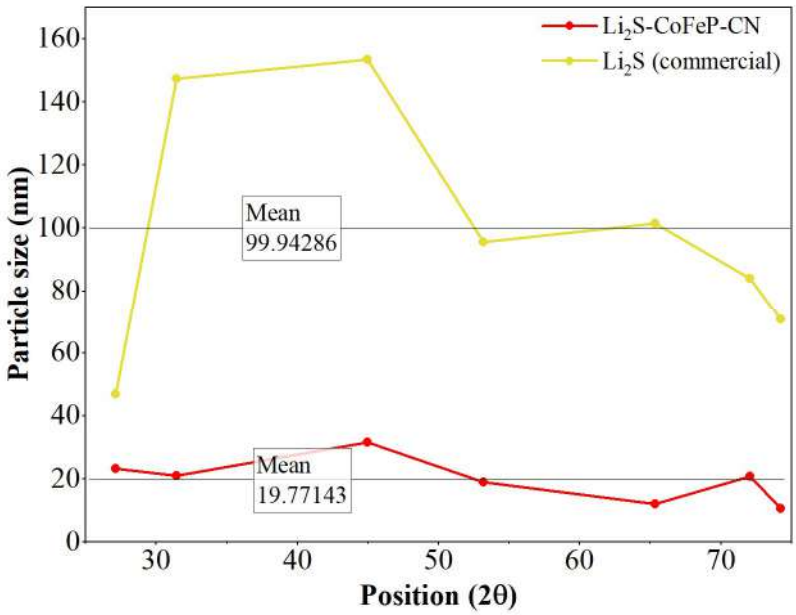


**Figure S3.** Crystallite size of $Li_2S$ calculated using Scherrer's formula considering different XRD peaks.

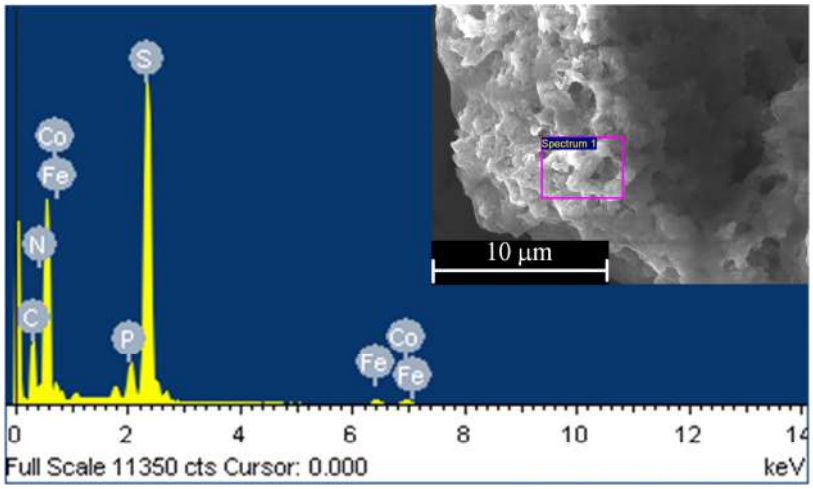


**Figure S4.** SEM-EDX spectrum of $Li_2S$-CoFeP-CN composite.

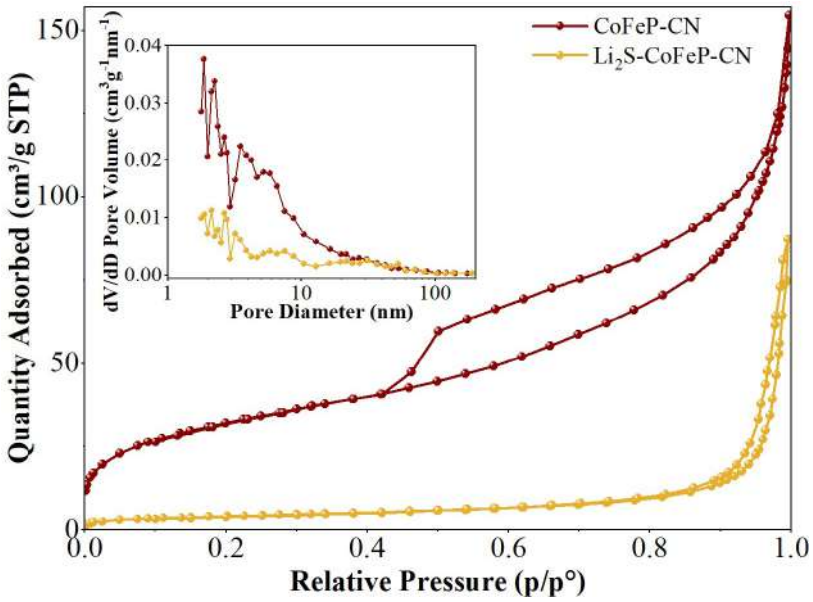


**Figure S5.** $N_2$ adsorption-desorption isotherms and pore size distribution (inset) of CoFeP-CN and $Li_2S$-CoFeP-CN.

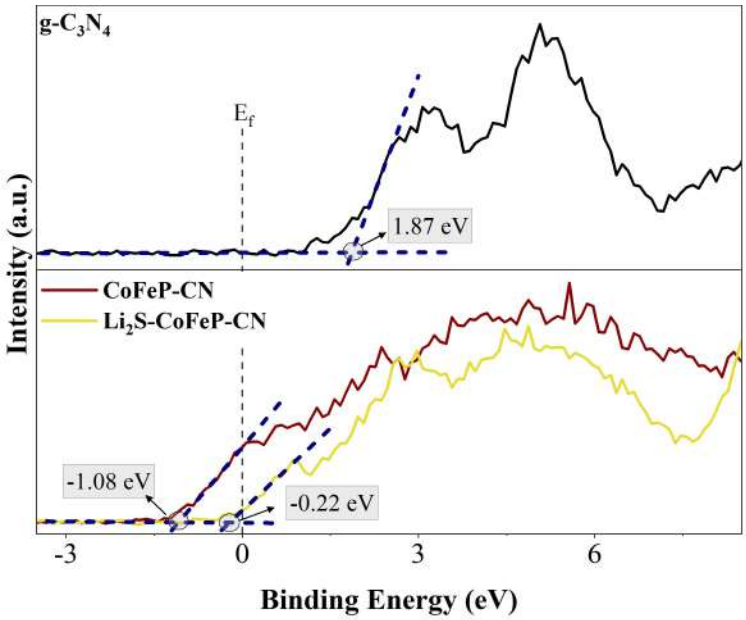


**Figure S6.** XPS valence band spectra of g-$C_3N_4$, CoFeP-CN, and $Li_2S$-CoFeP-CN.

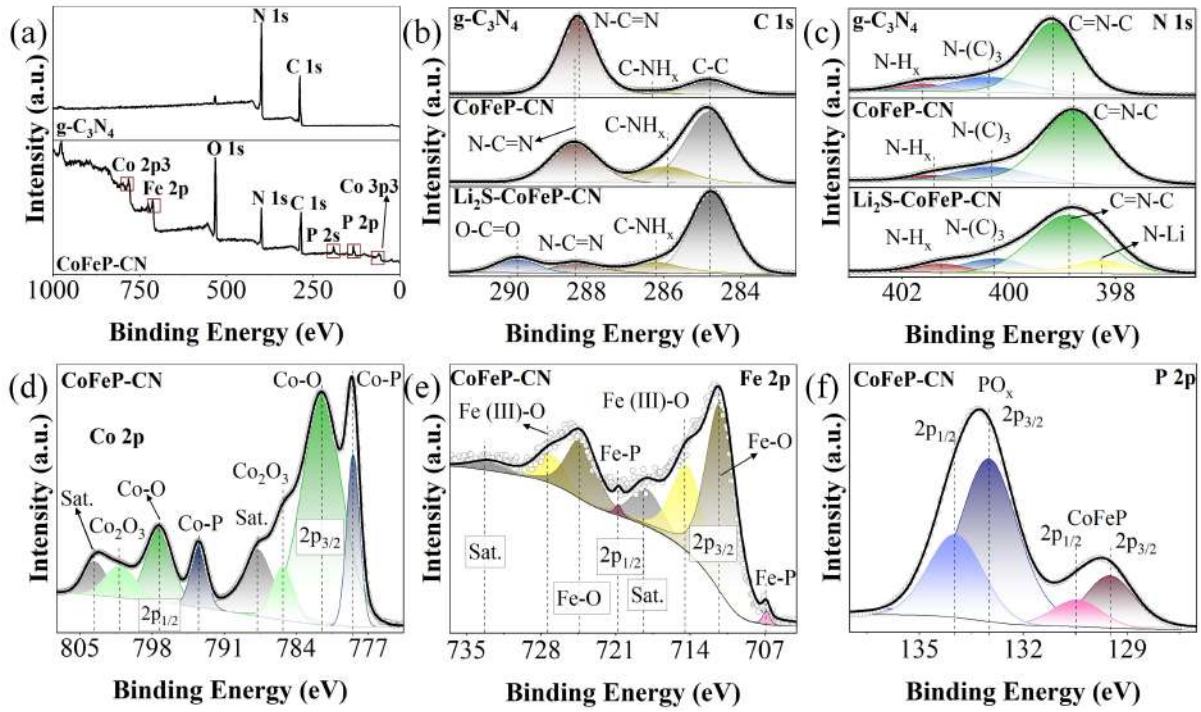


**Figure S7.** (a) XPS survey spectrum of g-$C_3N_4$ and CoFeP-CN. High resolution XPS spectra of g-$C_3N_4$, CoFeP-CN, and $Li_2S$-CoFeP-CN: (b) C 1s; (c) N 1s. High resolution XPS spectra of CoFeP-CN: (d) Co 2p; (e) Fe 2p; (f) P 2p.

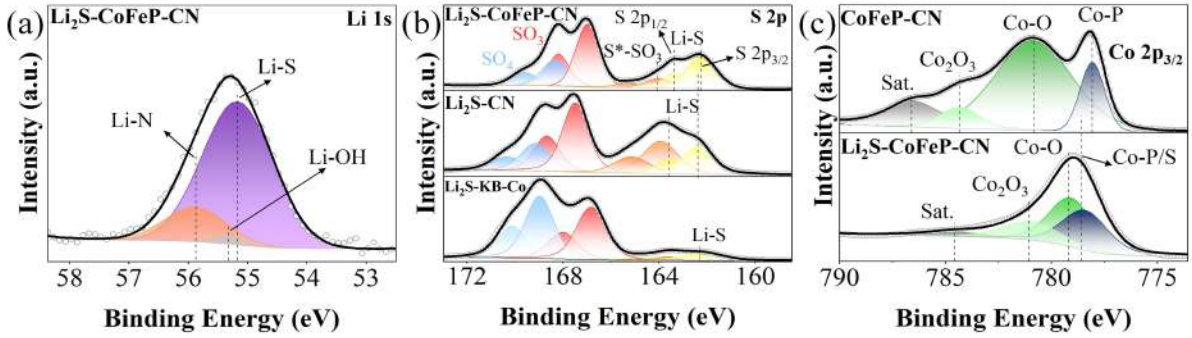


**Figure S8.** (a) Li 1s high resolution XPS spectra of $Li_2S$-CoFeP-CN. (b) S 2p high resolution XPS spectra of $Li_2S$-CoFeP-CN, $Li_2S$-CN, and $Li_2S$-KB-Co. (c) Co $2p_{3/2}$ high resolution XPS spectra of CoFeP-CN and $Li_2S$-CoFeP-CN.

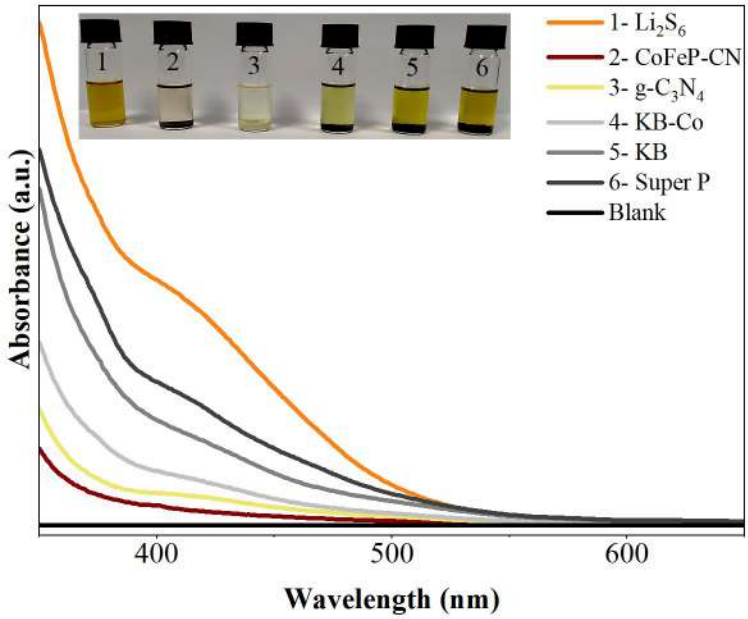


**Figure S9.** UV-vis absorption spectra of a $Li_2S_6$ solution and $Li_2S_6$ solutions containing different adsorbers after 12 h. The inset shows the digital photos of the $Li_2S_6$ solution and the LiPS adsorption ability of different adsorbers.

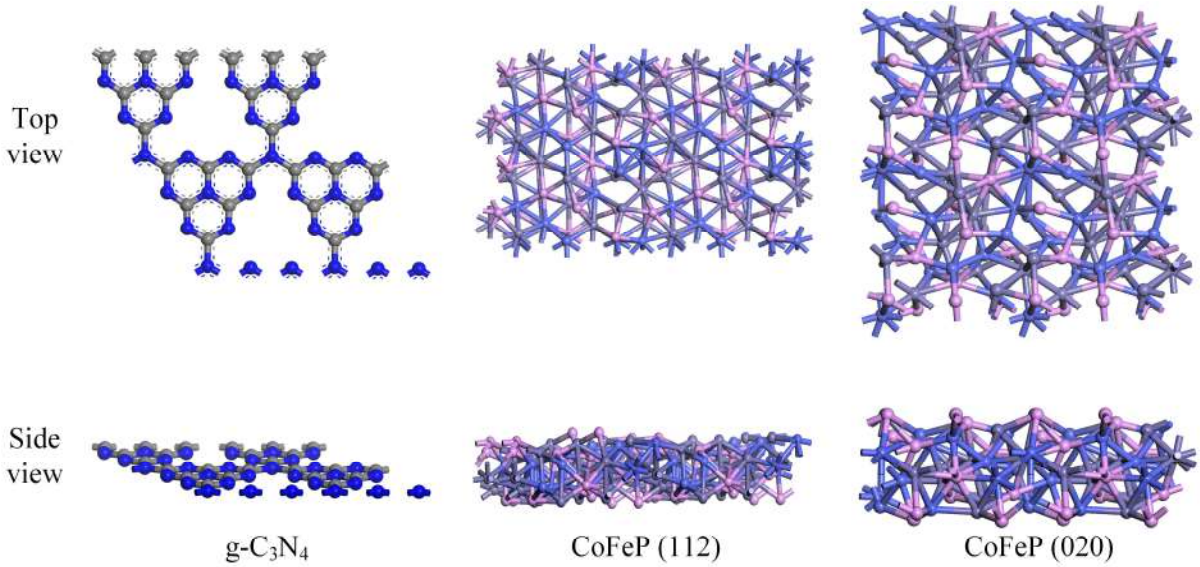


**Figure S10.** Top and side view of DFT models for g-$C_3N_4$ and different CoFeP surfaces.

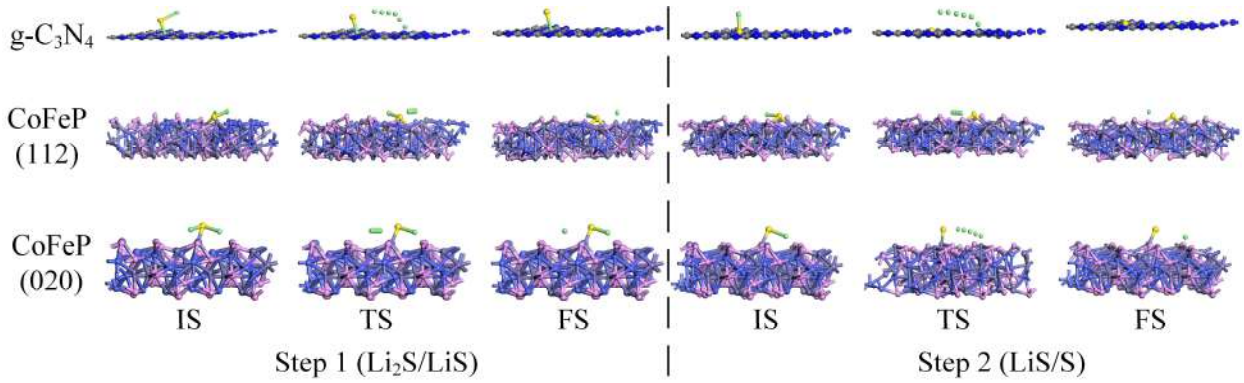


**Figure S11.** Side views of DFT models and decomposition pathways of $Li_2S$ on g-$C_3N_4$, CoFeP (112), and CoFeP (020). IS, TS, and FS stand for initial state, transition state, and final state, respectively.

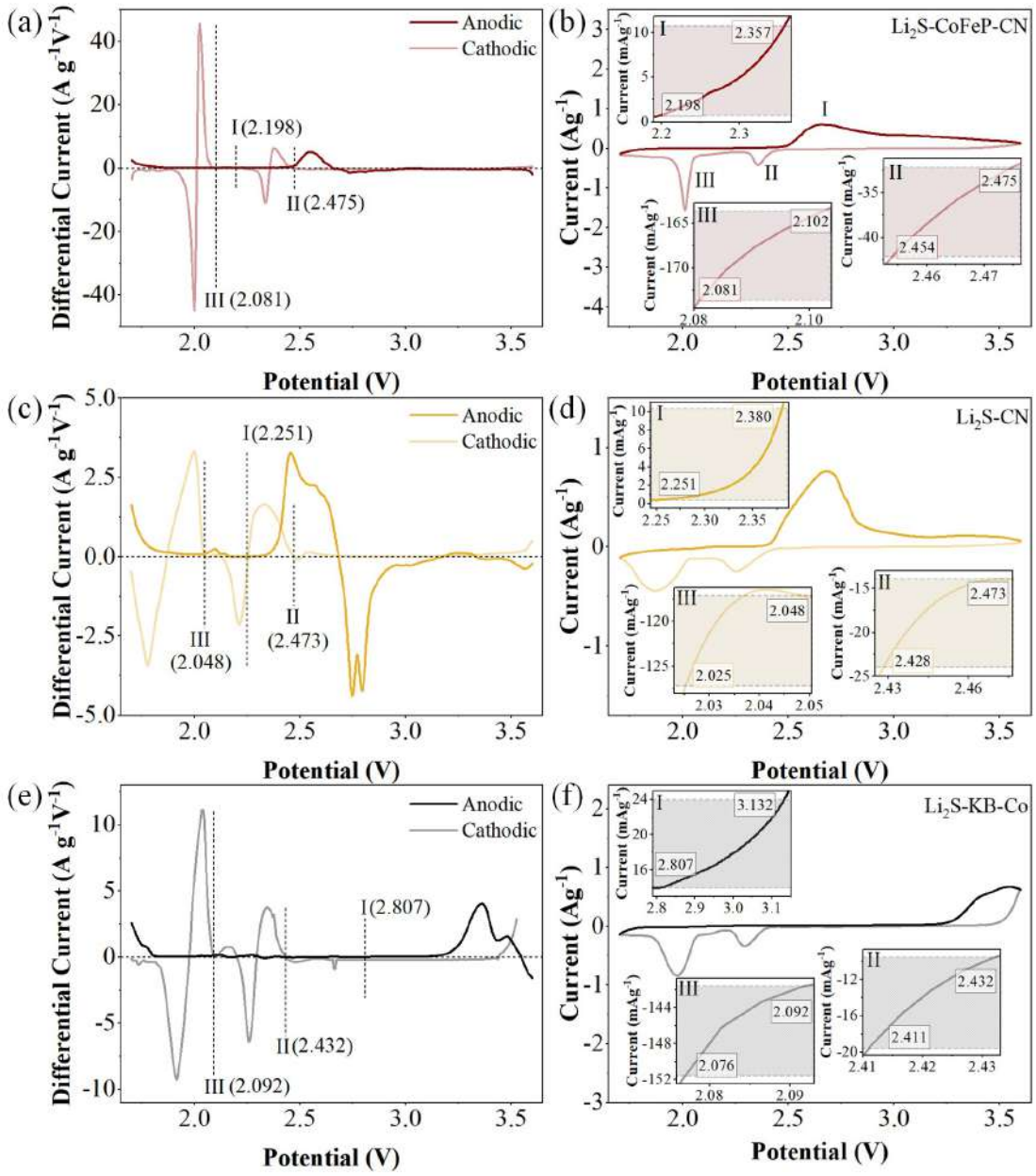


**Figure S12.** Onset potential of anodic peak (I) and cathodic peaks (II and III) for the activation cycle: (a, c, e) Differential CV curves and (b, d, f) CV curves with the corresponding onset potentials of redox peaks (inset) of $Li_2S$-CoFeP-CN, $Li_2S$-CN, and $Li_2S$-KB-Co. The baseline potentials and current densities were established as the value before the redox peak, where the dI/dV = 0.

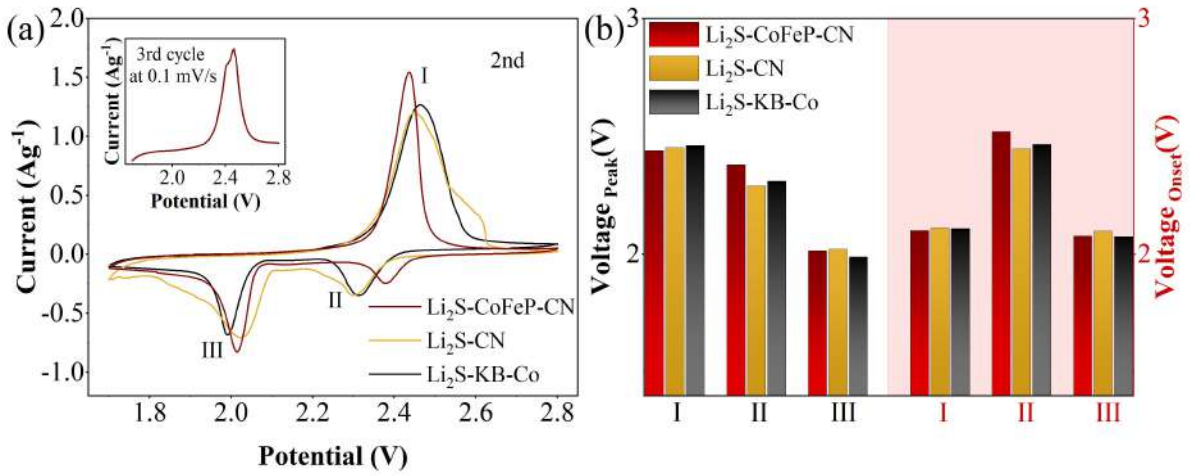


**Figure S13.** (a) CV curves of $Li_2S$-CoFeP-CN, $Li_2S$-CN, and $Li_2S$-KB-Co electrodes after the activation cycle at a scanning rate of 0.1 mV $s^{-1}$ between 1.7 and 2.8 V. Inset shows the anodic peak of the CV profile in the 3rd cycle at a scanning rate of 0.1 mV $s^{-1}$ for $Li_2S$-CoFeP-CN electrode. (b) Peak voltages and onset potentials obtained from CV curves of different electrodes.

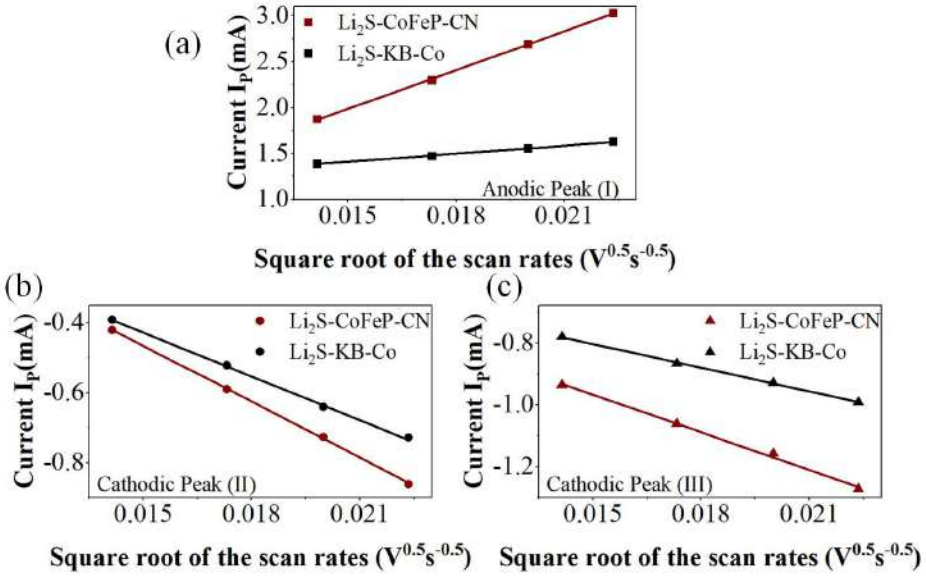


**Figure S14.** CV peak currents versus the square root of the scan rates calculated from CV results of $Li_2S$-CoFeP-CN electrode for (a) anodic peak I, (b) cathodic peak II, and (c) cathodic peak III.

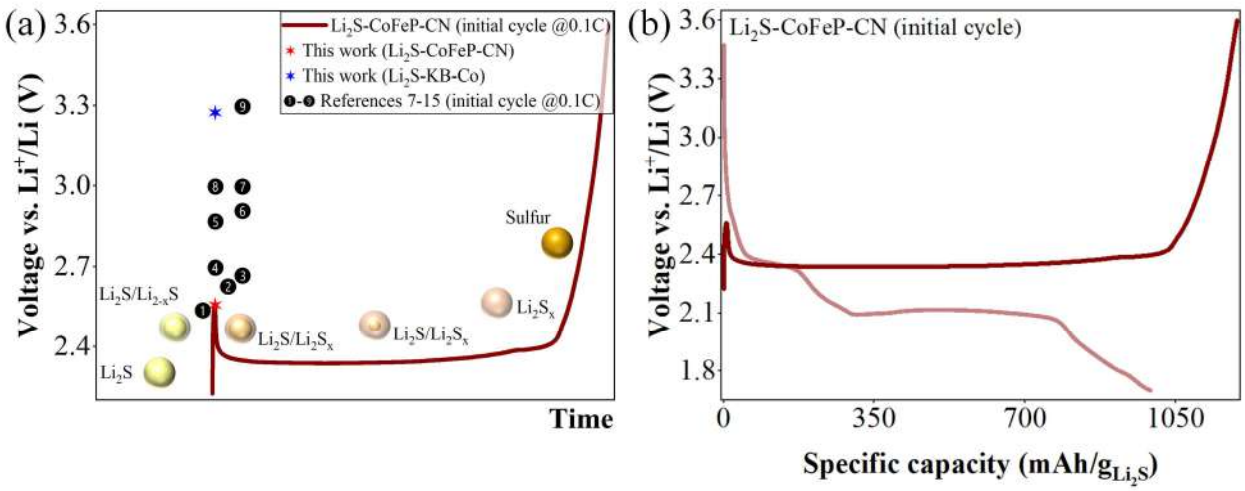


**Figure S15.** (a) Schematic of $Li_2S$ activation in the first charge process of $Li_2S$-CoFeP-CN electrode and comparison of activation barrier in $Li_2S$-CoFeP-CN with previously reported references.[7-15] (b) Initial charging-discharging profiles of $Li_2S$-CoFeP-CN at a current rate of 0.1C.

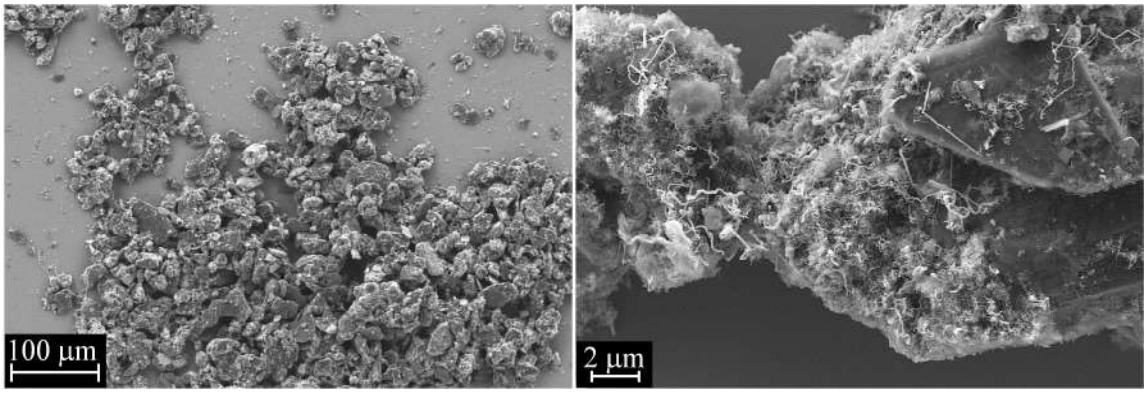


**Figure S16.** SEM images of Gt-SiNW with different magnifications.

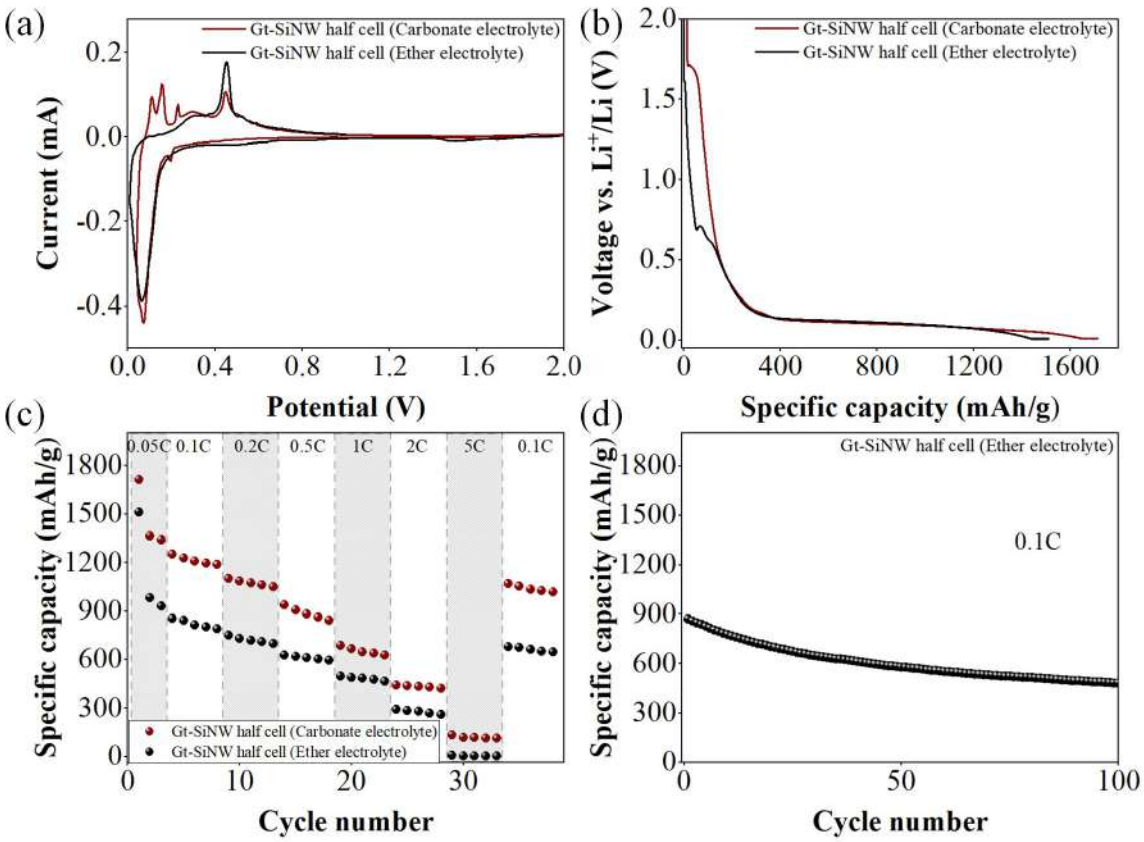


**Figure S17.** (a) CV curves of Gt-SiNW with carbonate-based electrolyte (1.2 M $LiPF_6$ in EC/DMC/EMC (2/3/5 vol%) containing 2wt.% VC, 2wt.% FEC) and ether-based electrolyte (1.0 M LiTFSI in DME/ DOL (v/v = 1/1) and 0.2 M of $LiNO_3$). (b) Initial discharging curves of Gt-SiNW half cell in different electrolytes. (c) C-rate performances of Gt-SiNW in different electrolytes. (d) Cycling performances of Gt-SiNW at 0.1 C with ether-based electrolyte.

**Table S1.** Elemental analysis of CoFeP-CN and $Li_2S$-CoFeP-CN obtained from large area EDX measurement.

| | | Li | S | C | N | Co | Fe | P |
|---|---|---|---|---|---|---|---|---|
| CoFeP-CN | at.% (measured) | – | – | 40 | 55 | 1.4 | 1.0 | 2.1 |
| | wt.% (measured) | – | – | 33 | 53 | 5.7 | 3.9 | 4.4 |
| $Li_2S$-CoFeP-CN | at.% (measured) | – | 41 | 25 | 31 | 0.8 | 0.6 | 1.0 |
| | wt.% (calculated) | 21 | 48 | 11 | 16 | 1.6 | 1.2 | 1.2 |
| | Composition | 69 wt.% $Li_2S$ | | 27 wt.% g-$C_3N_4$ | | 4.0 wt.% CoFeP | | |

**Table S2.** The EIS fitting results of the $Li_2S$-CoFeP-CN and the $Li_2S$-KB-Co electrodes based on the proposed equivalent circuit model.

| | $R_e$ (ohm) | $R_{(sf+ct)}$ (ohm) |
|---|---|---|
| $Li_2S$-CoFeP-CN (fresh cell) | 1.5 | 36 |
| $Li_2S$-CoFeP-CN (after cycling) | 3.3 | 10 |
| $Li_2S$-KB-Co (fresh cell) | 3.4 | 88 |

**Table S3.** A survey of electrochemical performances of $Li_2S$-based cathodes.

| | Cathodes | $Li_2S$ loading ($mg_{Li_2S}cm^{-2}$) | $Li_2S$ wt.% | Activation barrier@rate (1C=1166 mA $g^{-1}$) | Initial discharge capacity (mAh $g^{-1}$)@ rate | Discharge capacity (mAh $g^{-1}$)@ cycles number | Capacity retention (%) | Decay rate (% per cycle) |
|---|---|---|---|---|---|---|---|---|
| Recrystallization of $Li_2S$ | $Li_2S$-CoFeP-CN[This work] | 1.2 | 65-67 | 2.56@0.1C | 991@0.1C | — | — | — |
| | | | | | 756@0.2C | 641@150 | 84.7 | 0.1 |
| | | | | | 619@1C | 600 @100 | 97 | 0.03 |
| | | | | | | 543@400 | 88 | 0.03 |
| | | | | | | 472@800 | 76 | 0.029 |
| | $Li_2S$-CN[This work] | 1.2 | 65-67 | 2.51@0.1C | 770@0.1C | — | — | — |
| | | | | | 489@0.2C | 323@150 | 66 | 0.22 |
| | $Li_2S$-KB-Co[This work] | 1.2 | 65-67 | 3.28@0.1C | 830@0.1C | — | — | — |
| | | | | | 524@0.2C | 361@150 | 69 | 0.21 |
| | | | | | 395@1C | 331@100 | 84 | 0.16 |
| | | | | | | 241@400 | 61 | 0.098 |
| | $Li_2S$/CNT/GO/PPy[7] | 1.5 (the mass loading of electrode) | 64.7 | ~2.54@0.1C | 708@2C | 525@400 | 74.1 | 0.065 |
| | 3D $Li_2S$/p-$C_3N_4$/CNT[16] | 1.2 (the mass loading of electrode) | — | —@0.043C | 997.5@0.17C (200 mA$g^{-1}$) | 782.9@60 | 78.5 | 0.36 |
| | | | | | 932.3@0.43C (500 mA$g^{-1}$) | 652.8@200 | 70 | 0.15 |
| | $Li_2S$@honeycomb-like nitrogen-doped carbon[17] | 1.4 | 40 | — | 1020@0.1C | 815@65 | 80 | 0.31 |
| | $Li_2S$@MXene/G[18] | 3 | 62 | 2.41@0.2C | 710@0.2C | 615.6@100 | 86.7 | 0.13 |

| | | | | | | | | |
|---|---|---|---|---|---|---|---|---|
| | $Li_2S/Ti_3C_2T_X$[19] | 1.6 (the mass loading of electrode) | — | 2.71@0.05C | 708@0.1C | 528@100 | 74.5 | 0.25 |
| | Vertical-Aligned graphene/$Li_2S$-C[20] | 1.84 | — | — | 890@0.1C | 656@100 | 73 | 0.26 |
| | rGO-$Li_2S$@C[21] | 2.5-3.5 | 75 | —@0.025C | 856@0.1C | 563@100 | 65.7 | 0.34 |
| | Free-standing flexible electrode[22] | 1.3 | 50 | — | 878@0.5C | 696@400 | 77 | 0.058 |
| | $Li_2S$@N-rich carbon[23] | 1.53 | 63 | ~2.5@0.05C | 1046@0.25C | 771@100 | 74 | 0.26 |
| | | | | | 958@0.5C | 565@500 | 59 | 0.041 @100 0 |
| | Graphene-$Li_2S$-Carbon[24] | ~0.61-1.31 | 55 | — | 748@0.2C | 724@700 | 97 | 0.004 |
| | $Li_2S$@C-Co-N[25] | 2 | 41.6 | — | 1137@0.2C | 929.6@300 | 81.7 | 0.06 |
| | Core-shell $Li_2S$@C[26] | 2.8 | 57.8 | —@0.2C | 754@0.2C | 533.5@200 | 70.7 | 0.15 |
| | | | | | 469.6@1C | 403.8@200 | 86 | 0.07 |
| | $Li_2S$/reduced graphene oxide[27] | 0.8-1.5 | 50-60 | — | 1119@0.1C | 816.1@150 | 73 | 0.18 |
| | C-$Li_2S$[28] | ~0.75 | 51 | 3.2@0.05C | 922@0.2C | 835@100 | 90 | 0.095 |
| | $Li_2S$/graphene[29] | 1 | 82 | 3.5@0.05C | 765@0.05C | — | — | — |
| | | | | | —@0.1C | —@200 | 83 | 0.085 |
| Other $Li_2S$ synthesis method | 3DP@$Li_2S$[30] | ~2.4 | — | 3.27@0.3C | 790@1C | 692@100 | 87 | 0.12 |
| | $Li_2S$@PC@CNF/CNF[15] | 2.66 (based on sulfur) | 47 | 3.3@0.1C | 700@0.2C | 500@400 | 71 | 0.071 |
| | $Li_2S$-CNF[31] | 2.3 (the mass loading of electrode) | — | —@0.2C | 895@0.2C | — | — | — |
| | | | | | 853.33@0.5C | 512@200 | 60 | 0.2 |
| | $Li_2S$-graphene[32] | 1 | 60 | —@0.05C | 600@0.5C | 405@400 | 67.5 | 0.08 |
| | $Li_2S$/C (with 500 ppm ethanol)[33] | 1.2-2 | 60 | 3.1@0.2C | 1144@0.2 C | 425@100 | 37 | 0.63 |
| | $Li_2S$-ZnS@NC[11] | 2 | 62.6 | 2.87@0.1C | 832@0.2C | 640.64@100 | 77 | 0.23 |
| | | | | | 665@1C | 525.35@100 0 | 79 | 0.021 |
| | nano-$Li_2S$/GA[13] | 3.6 | 69 | ~3.0@0.1C | 838.5@0.1C | 462.8@100 | 55.2 | 0.45 |
| | $Li_2S$-$TiS_2$[14] | 6 | 75 | 3@0.14C | 704@0.14C | 400@200 | 57 | 0.21 |
| | TiN/PHC@$Li_2S$[34] | 2.5-3.5 | 45 | ~2.85@0.05 C | 789@0.2C | 661@100 | 84 | 0.16 |
| | $Ti_3C_2/Li_2S$[35] | 0.8 | 60 | 2.85@0.2C | 700@0.2C | 440@100 | 63 | 0.37 |

| | | | | | | | |
|---|---|---|---|---|---|---|---|
| $Li_2S$-PAN[36] | 0.42-1.06 | 37 | — | 484@0.1C | 438.6@250 | 90.6 | 0.037 |
| $Li_2S$/CNT/C-N/O[37] | 2 | 60.2 | ~3@0.03C | 1014@0.03C | — | — | — |
| | | | | 713.83@0.2C | 671@200 | 94 | 0.03 |
| $Li_2S$@C-CNT[8] | 1.86 | — | 2.63@0.1C | 805@0.1C | — | — | — |
| | | | | 692@0.2C | 595@150 | 86 | 0.093 |
| $Li_2S$/N,P-C[10] | 2 (the mass loading of electrode) | 62 | 2.7@0.1C | 1000@0.1C | 700@100 | 70 | 0.1 |
| | | | | —@1C | 470@300 | — | — |
| $VS_2$-$Li_2S$[12] | 0.9-1.1 | — | 2.91@0.1C | 830@0.5C | 701@300 | 84.5 | 0.052 |
| $Li_2S$@porous carbon[38] | 1 | 70 | 3.75@0.05C | 772@0.05C | — | — | — |
| | | | | 410@1C | 252@200 | 61 | 0.19 |
| $Li_2S$–C NF[9] | ~0.9 | 72.2 | 2.57@0.025 | 800@0.025C | 510@100@0.5C | — | — |
| | | | 2.67@0.1C | | | | |
| Nitridated graphene-$Li_2S$[39] | 1.2 | 66.3 | —@0.05C | 1067@0.05C | 480@500@0.2 C | — | — |
| $Li_2S$@$TiS_2$[40] | ~1 | 51 | 3@0.05C | 806@0.2C | 693.16@150 | 86 | 0.093 |
| | | | | 666@0.5C | 513@400 | 77 | 0.058 |

**Table S4.** Elemental composition of Gt-SiNW composite by weight percent (%) and corresponding capacities of the materials.

| Elements/Composite | Content (wt. %) | Theoretical capacity (mAh $g^{-1}$) |
|---|---|---|
| Silicon | 25 | 3579 |
| Carbon | 71 | 350 |
| Tin | 4 | 993 |
| Gt-SiNW | 100 | 1182.97 |
| 1 C= 1.18297 A | | |

**Table S5.** Electrochemical test of Gt-SiNW half cell and Gt-SiNW/$Li_2S$-CoFeP-CN full cell protocol.

| C-rate test of Gt-SiNW half cell | | | Stability test of Gt-SiNW half cell | | | Prelithiation of Gt-SiNW half cell | | | Stability test of full cell (Gt-SiNW/$Li_2S$-CoFeP-CN) | | |
|---|---|---|---|---|---|---|---|---|---|---|---|
| Dis | C/20 (0.01 V) - CV (C/100,100h) | 3 | Dis | C/20 (0.01 V) - CV (C/100,100h) | 1 | Dis | C/20 (0.01 V) - CV (C/100,100h) | 1 | Ch | C/10 | 1 |
| Ch | C/20 (1 V) | | Ch | C/20 (1 V) | | | | | Dis | C/10 | |
| Dis | C/10, C/5, C/2, 1 C, 2 C, 5 C | 5 | Dis | C/10 | - | | | | Ch | C/5 | - |
| Ch | C/10, C/5, C/2, 1 C, 2 C, 5 C | | Ch | C/10 | | | | | Dis | C/5 | |

**Table S6.** Full cell information.

| | |
|---|---|
| Electrode area ($cm^2$) | 1.1309 |
| Gt-SiNW mass loading (mg $cm^{-2}$) | 3.265 |
| $Li_2S$-CoFeP-CN mass loading (mg $cm^{-2}$) | 1.4 |
| Initial Coulombic efficiency (%) | 71.9 |
| Coulombic efficiency at first cycle after activation ($2^{nd}$ cycle) (%) | 89.7 |
| Initial capacity density (mAh $g_{Li2S}^{-1}$) | 903 |
| First cycle capacity density ($2^{nd}$ cycle) (mAh $g_{Li2S}^{-1}$) | 805.6 |

## References


(1) Karuppiah, S.; Keller, C.; Kumar, P.; Jouneau, P. H.; Aldakov, D.; Ducros, J. B.; Lapertot, G.; Chenevier, P.; Haon, C. A Scalable Silicon Nanowires-Grown-on-Graphite Composite for High-Energy Lithium Batteries. *ACS Nano* **2020**, *14* (9), 12006-12015. DOI: 10.1021/acsnano.0c05198 From NLM PubMed-not-MEDLINE.

(2) Keller, C.; Karuppiah, S.; Raaen, M.; Wang, J.; Perrenot, P.; Aldakov, D.; Reiss, P.; Haon, C.; Chenevier, P. Low-Cost Tin Compounds as Seeds for the Growth of Silicon Nanowire–Graphite Composites Used in High-Performance Lithium-Ion Battery Anodes. *ACS Appl. Energy Mater.* **2023**, *6* (10), 5249-5258. DOI: 10.1021/acsaem.3c00178.

(3) Keller, C.; Djezzar, Y.; Wang, J.; Karuppiah, S.; Lapertot, G.; Haon, C.; Chenevier, P. Easy Diameter Tuning of Silicon Nanowires with Low-Cost $SnO_2$-Catalyzed Growth for Lithium-Ion Batteries. *Nanomaterials* **2022**, *12* (15). DOI: 10.3390/nano12152601 From NLM PubMed-not-MEDLINE.

(4) Perdew, J. P.; Burke, K.; Ernzerhof, M. Generalized Gradient Approximation Made Simple. *Phys. Rev. Lett.* **1996**, *77* (18), 3865-3868. DOI: 10.1103/PhysRevLett.77.3865 From NLM Publisher.

(5) Kresse, G.; Hafner, J. Norm-Conserving and Ultrasoft Pseudopotentials for First-Row and Transition Elements. *J. Phys.: Condens. Matter* **1994**, *6* (40), 8245-8257. DOI: 10.1088/0953-8984/6/40/015.

(6) Monkhorst, H. J.; Pack, J. D. Special Points for Brillouin-Zone Integrations. *Phys. Rev. B* **1976**, *13* (12), 5188-5192. DOI: 10.1103/PhysRevB.13.5188.

(7) Liu, H.; Zeng, P.; Yu, H.; Zhou, X.; Li, Z.; Chen, M.; Miao, C.; Chen, G.; Wu, T.; Wang, X. Enhancing the Electrochemical Performances of $Li_2S$-Based Cathode through Conductive Interface Design and Addition of Mixed Conductive Materials. *Electrochim. Acta* **2021**, *396*. DOI: 10.1016/j.electacta.2021.139238.

(8) Ye, F.; Noh, H.; Lee, J.; Lee, H.; Kim, H.-T. $Li_2S$/Carbon Nanocomposite Strips from a Low-Temperature Conversion of $Li_2SO_4$ as High-Performance Lithium–Sulfur Cathodes. *J. Mater. Chem. A* **2018**, *6* (15), 6617-6624. DOI: 10.1039/c8ta00515j.

(9) Ye, F.; Hou, Y.; Liu, M.; Li, W.; Yang, X.; Qiu, Y.; Zhou, L.; Li, H.; Xu, Y.; Zhang, Y. Fabrication of Mesoporous $Li_2S$-C Nanofibers for High Performance Li/$Li_2S$ Cell Cathodes. *Nanoscale* **2015**, *7* (21), 9472-9476. DOI: 10.1039/c5nr00480b From NLM PubMed-not-MEDLINE.

(10) Zhang, J.; Shi, Y.; Ding, Y.; Peng, L.; Zhang, W.; Yu, G. A Conductive Molecular Framework Derived $Li_2S$/N,P-Codoped Carbon Cathode for Advanced Lithium–Sulfur Batteries. *Adv. Energy Mater.* **2017**, *7* (14). DOI: 10.1002/aenm.201602876.

(11) Yu, M.; Zhou, S.; Wang, Z.; Pei, W.; Liu, X.; Liu, C.; Yan, C.; Meng, X.; Wang, S.; Zhao, J.; Qiu, J. A Molecular-Cage Strategy Enabling Efficient Chemisorption–Electrocatalytic Interface in Nanostructured $Li_2S$ Cathode for Li Metal-Free Rechargeable Cells with High Energy. *Adv. Funct. Mater.* **2019**, *29* (46). DOI: 10.1002/adfm.201905986.

(12) Zhou, G.; Tian, H.; Jin, Y.; Tao, X.; Liu, B.; Zhang, R.; Seh, Z. W.; Zhuo, D.; Liu, Y.; Sun, J.; Zhao, J.; Zu, C.; Wu, D. S.; Zhang, Q.; Cui, Y. Catalytic Oxidation of $Li_2S$ on the Surface of Metal Sulfides for Li-S Batteries. *PNAS* **2017**, *114* (5), 840-845. DOI: 10.1073/pnas.1615837114 From NLM PubMed-not-MEDLINE.

(13) Wang, Z.; Xu, C.; Chen, L.; Si, J.; Li, W.; Huang, S.; Jiang, Y.; Chen, Z.; Zhao, B. In-Situ Lithiation Synthesis of Nano-Sized Lithium Sulfide/Graphene Aerogel with Covalent Bond Interaction for Inhibiting the Polysulfides Shuttle of Li-S Batteries. *Electrochim. Acta* **2019**, *312*, 282-290. DOI: 10.1016/j.electacta.2019.04.169.

(14) Chung, S. H.; Manthiram, A. A $Li_2S$-$TiS_2$-Electrolyte Composite for Stable $Li_2S$-Based Lithium–Sulfur Batteries. *Adv. Energy Mater.* **2019**, *9* (30). DOI: 10.1002/aenm.201901397.

(15) Li, S.; Jiang, J.; Dong, Z.; Wu, J.; Cheng, Z.; Zhu, H.; Fan, Z.; Wang, Y.; Leng, D. Ferroconcrete-Inspired Construction of Self-Supporting $Li_2S$ Cathode for High-Performance Lithium–Sulfur Batteries. *Microporous Mesoporous Mater.* **2020**, *293*. DOI: 10.1016/j.micromeso.2019.109822.

(16) Liang, S.; Chen, J.; Zhou, N.; Hu, L.; Liu, L.; Wang, L.; Liang, D.; Yu, T.; Tian, C.; Liang, C. Cnt Threaded Porous Carbon Nitride Nanoflakes as Bifunctional Hosts for Lithium Sulfide Cathode. *J. Alloys Compd.* **2021**, *887*. DOI: 10.1016/j.jallcom.2021.161356.

(17) Kim, Y.; Han, H.; Noh, Y.; Bae, J.; Ham, M. H.; Kim, W. B. Honeycomb-Like Nitrogen-Doped Carbon 3D Nanoweb@$Li_2S$ Cathode Material for Use in Lithium Sulfur Batteries. *ChemSusChem* **2019**, *12* (4), 824-829. DOI: 10.1002/cssc.201802698 From NLM PubMed-not-MEDLINE.

(18) Wang, Z.; Zhang, N.; Yu, M.; Liu, J.; Wang, S.; Qiu, J. Boosting Redox Activity on Mxene-Induced Multifunctional Collaborative Interface in High $Li_2S$ Loading Cathode for High-Energy Li-S and Metallic Li-Free Rechargeable Batteries. *J. Energy Chem.* **2019**, *37*, 183-191. DOI: 10.1016/j.jechem.2019.03.012.

(19) Pourali, Z.; Yaftian, M. R.; Sovizi, M. R. $Li_2S$/Transition Metal Carbide Composite as Cathode Material for High Performance Lithium-Sulfur Batteries. *Mater. Chem. Phys.* **2018**, *217*, 117-124. DOI: 10.1016/j.matchemphys.2018.06.074.

(20) Wang, D.; Xia, X.; Wang, Y.; Xie, D.; Zhong, Y.; Wu, J.; Wang, X.; Tu, J. Vertical-Aligned $Li_2S$-Graphene Encapsulated within a Carbon Shell as a Free-Standing Cathode for Lithium-Sulfur Batteries. *Chemistry* **2017**, *23* (46), 11169-11174. DOI: 10.1002/chem.201702779 From NLM PubMed-not-MEDLINE.

(21) Wang, D. H.; Xie, D.; Yang, T.; Zhong, Y.; Wang, X. L.; Xia, X. H.; Gu, C. D.; Tu, J. P. $Li_2S$@C Composite Incorporated into 3D Reduced Graphene Oxide as a Cathode Material for Lithium-Sulfur Batteries. *J. Power Sources* **2016**, *313*, 233-239. DOI: 10.1016/j.jpowsour.2016.03.001.

(22) Wu, F.; Zhao, E.; Gordon, D.; Xiao, Y.; Hu, C.; Yushin, G. Infiltrated Porous Polymer Sheets as Free-Standing Flexible Lithium-Sulfur Battery Electrodes. *Adv. Mater.* **2016**, *28* (30), 6365-6371. DOI: 10.1002/adma.201600757 From NLM PubMed-not-MEDLINE.

(23) Hu, C.; Chen, H.; Xie, Y.; Fang, L.; Fang, J.; Xu, J.; Zhao, H.; Zhang, J. Alleviating Polarization by Designing Ultrasmall $Li_2S$ Nanocrystals Encapsulated in N-Rich Carbon as a Cathode Material for High-Capacity, Long-Life Li–S Batteries. *J. Mater. Chem. A* **2016**, *4* (47), 18284-18288. DOI: 10.1039/c6ta08572e.

(24) Wu, F.; Lee, J. T.; Zhao, E.; Zhang, B.; Yushin, G. Graphene-$Li_2S$-Carbon Nanocomposite for Lithium-Sulfur Batteries. *ACS Nano* **2016**, *10* (1), 1333-1340. DOI: 10.1021/acsnano.5b06716 From NLM PubMed-not-MEDLINE.

(25) He, J.; Chen, Y.; Lv, W.; Wen, K.; Xu, C.; Zhang, W.; Li, Y.; Qin, W.; He, W. From Metal-Organic Framework to $Li_2S$@C-Co-N Nanoporous Architecture: A High-Capacity Cathode for Lithium-Sulfur Batteries. *ACS Nano* **2016**, *10* (12), 10981-10987. DOI: 10.1021/acsnano.6b05696 From NLM PubMed-not-MEDLINE.

(26) Yang, T.; Wang, X.; Wang, D.; Li, S.; Xie, D.; Zhang, X.; Xia, X.; Tu, J. Facile and Scalable Synthesis of Nanosized Core–Shell $Li_2S$@C Composite for High-Performance Lithium–Sulfur Batteries. *J. Mater. Chem. A* **2016**, *4* (42), 16653-16660. DOI: 10.1039/c6ta06361f.

(27) Wang, C.; Wang, X.; Yang, Y.; Kushima, A.; Chen, J.; Huang, Y.; Li, J. Slurryless $Li_2S$/Reduced Graphene Oxide Cathode Paper for High-Performance Lithium Sulfur Battery. *Nano Lett* **2015**, *15* (3), 1796-1802. DOI: 10.1021/acs.nanolett.5b00112 From NLM PubMed-not-MEDLINE.

(28) Wu, F.; Kim, H.; Magasinski, A.; Lee, J. T.; Lin, H.-T.; Yushin, G. Harnessing Steric Separation of Freshly Nucleated $Li_2S$ Nanoparticles for Bottom-up Assembly of High-Performance Cathodes for Lithium-Sulfur and Lithium-Ion Batteries. *Adv. Energy Mater.* **2014**, *4* (11). DOI: 10.1002/aenm.201400196.

(29) Wu, F.; Lee, J. T.; Magasinski, A.; Kim, H.; Yushin, G. Solution-Based Processing of Graphene-$Li_2S$ Composite Cathodes for Lithium-Ion and Lithium-Sulfur Batteries. *Part. Part. Syst. Char.* **2014**, *31* (6), 639-644. DOI: 10.1002/ppsc.201300358.

(30) Xue, L.; Zeng, L.; Kang, W.; Chen, H.; Hu, Y.; Li, Y.; Chen, W.; Lei, T.; Yan, Y.; Yang, C.; Hu, A.; Wang, X.; Xiong, J.; Zhang, C. 3D Printed Li–S Batteries with in Situ Decorated $Li_2S$/C Cathode: Interface Engineering Induced Loading-Insensitivity for Scaled Areal Performance. *Adv. Energy Mater.* **2021**, *11* (14). DOI: 10.1002/aenm.202100420.

(31) Wu, D. S.; Zhou, G.; Mao, E.; Sun, Y.; Liu, B.; Wang, L.; Wang, J.; Shi, F.; Cui, Y. A Novel Battery Scheme: Coupling Nanostructured Phosphorus Anodes with Lithium Sulfide Cathodes. *Nano Res.* **2020**, *13* (5), 1383-1388. DOI: 10.1007/s12274-020-2645-8.

(32) Shi, P.; Liang, X.; Xu, K.; Sun, Y.; Cheng, S.; Chen, C.; Xiang, H. Sulfone-Assisted-$NH_4I$ as Electrolyte Additive with Synergistic Dissolution and Catalysis Effects on Reducing the Activation Voltage of $Li_2S$ Cathode. *Chem. Eng. J.* **2020**, *398*. DOI: 10.1016/j.cej.2020.125608.

(33) Liang, X.; Yun, J.; Xu, K.; Shi, P.; Sun, Y.; Chen, C.; Xiang, H. Trace Ethanol as an Efficient Electrolyte Additive to Reduce the Activation Voltage of the $Li_2S$ Cathode in Lithium-Ion-Sulfur Batteries. *Chem. Commun.* **2019**, *55* (68), 10088-10091. DOI: 10.1039/c9cc04877d From NLM PubMed-not-MEDLINE.

(34) Hao, Z.; Chen, J.; Yuan, L.; Bing, Q.; Liu, J.; Chen, W.; Li, Z.; Wang, F. R.; Huang, Y. Advanced $Li_2S$/Si Full Battery Enabled by Tin Polysulfide Immobilizer. *Small* **2019**, *15* (50), e1902377. DOI: 10.1002/smll.201902377 From NLM PubMed-not-MEDLINE.

(35) Liang, X.; Yun, J.; Xu, K.; Xiang, H.; Wang, Y.; Sun, Y.; Yu, Y. A Multi-Layered $Ti_3C_2/Li_2S$ Composite as Cathode Material for Advanced Lithium-Sulfur Batteries. *J. Energy Chem.* **2019**, *39*, 176-181. DOI: 10.1016/j.jechem.2019.02.002.

(36) Shen, Y.; Zhang, J.; Pu, Y.; Wang, H.; Wang, B.; Qian, J.; Cao, Y.; Zhong, F.; Ai, X.; Yang, H. Effective Chemical Prelithiation Strategy for Building a Silicon/Sulfur Li-Ion Battery. *ACS Energy Lett.* **2019**, *4* (7), 1717-1724. DOI: 10.1021/acsenergylett.9b00889.

(37) Peng, Y.; Zhang, Y.; Wen, Z.; Wang, Y.; Chen, Z.; Hwang, B.-J.; Zhao, J. Constructing Fast Electron and Ion Conductive Framework for $Li_2S$ as Advanced Lithium Sulfur Battery. *Chem. Eng. J.* **2018**, *346*, 57-64. DOI: 10.1016/j.cej.2018.04.049.

(38) Wang, N.; Zhao, N.; Shi, C.; Liu, E.; He, C.; He, F.; Ma, L. In Situ Synthesized $Li_2S$@Porous Carbon Cathode for Graphite/$Li_2S$ Full Cells Using Ether-Based Electrolyte. *Electrochim. Acta* **2017**, *256*, 348-356. DOI: 10.1016/j.electacta.2017.10.053.

(39) Qiu, Y.; Rong, G.; Yang, J.; Li, G.; Ma, S.; Wang, X.; Pan, Z.; Hou, Y.; Liu, M.; Ye, F.; Li, W.; Seh, Z. W.; Tao, X.; Yao, H.; Liu, N.; Zhang, R.; Zhou, G.; Wang, J.; Fan, S.; Cui, Y.; Zhang, Y. Highly Nitridated Graphene-$Li_2S$ Cathodes with Stable Modulated Cycles. *Adv. Energy Mater.* **2015**, *5* (23). DOI: 10.1002/aenm.201501369.

(40) Seh, Z. W.; Yu, J. H.; Li, W.; Hsu, P. C.; Wang, H.; Sun, Y.; Yao, H.; Zhang, Q.; Cui, Y. Two-Dimensional Layered Transition Metal Disulphides for Effective Encapsulation of High-Capacity Lithium Sulphide Cathodes. *Nat. Commun.* **2014**, *5*, 5017. DOI: 10.1038/ncomms6017 From NLM PubMed-not-MEDLINE.